Modeling the speciation and biogeochemistry of iron at the Bermuda Atlantic Time-series Study site

L. Weber[1]
Leibniz Institut für Meereswissenschaften an der Universität Kiel, Germany

C. Völker, M. Schartau,[2] and D. A. Wolf-Gladrow
Alfred-Wegener-Institut für Polar- und Meeresforschung, Bremerhaven, Germany

Received 16 July 2004; revised 17 December 2004; accepted 17 January 2005; published 16 March 2005.

[1] By means of numerical modeling, we analyze the cycling of iron between its various physical (dissolved, colloidal, particulate) and chemical (redox state and organic complexation) forms in the upper mixed layer. With our proposed model it is possible to obtain a first quantitative assessment of how this cycling influences iron uptake by phytoplankton and its loss via particle export. The model is forced with observed dust deposition rates, mixed layer depths, and solar radiation at the site of the Bermuda Atlantic Time-series Study (BATS). It contains an objectively optimized ecosystem model which yields results close to the observational data from BATS that has been used for the data-assimilation procedure. It is shown that the mixed layer cycle strongly influences the cycling of iron between its various forms. This is mainly due to the light dependency of photoreductive processes, and to the seasonality of primary production. The daily photochemical cycle is driven mainly by the production of superoxide, and its amplitude depends on the concentration and speciation of dissolved copper. Model results are almost insensitive to the dominant form of dissolved iron within dust deposition, and also to the form of iron that is taken up directly during algal growth. In our model solutions, the role of the colloidal pumping mechanism depends strongly on assumptions on the colloid aggregation and photoreduction rate.

Citation: Weber, L., C. Völker, M. Schartau, and D. A. Wolf-Gladrow (2005), Modeling the speciation and biogeochemistry of iron at the Bermuda Atlantic Time-series Study site, *Global Biogeochem. Cycles*, *19*, GB1019, doi:10.1029/2004GB002340.

1. Introduction

[2] The role of iron for phytoplankton productivity in the ocean has received much attention over the last years. Iron is an important micro-nutrient for phytoplankton, being required notably for photosynthesis and the assimilation of nitrogen [*Geider and La Roche*, 1994; *Armstrong*, 1999]. Low supply rates of iron to the upper ocean from dust deposition [*Duce and Tindale*, 1991] and upwelling [*Fung et al.*, 2000] have been made responsible for the persistence of high-nitrate low-chlorophyll (HNLC) conditions in the Southern Ocean, the equatorial Pacific, and the subpolar North Pacific [*Martin and Fitzwater*, 1988]. In these areas the macro-nutrients nitrate and phosphate are abundant without causing phytoplankton blooms. This so-called iron hypothesis [*Martin*, 1990] has since been supported by the outcomes of a number of laboratory and field experiments, most prominently several large-scale iron fertilization experiments [e.g., *Martin et al.*, 1994; *Coale et al.*, 1996; *Boyd and Law*, 2001].

[3] However, in these and other experiments, the speciation of iron has increasingly been recognized as an additional controlling factor [*Wells*, 2003]. Iron in seawater exists in a variety of chemical and physical forms, including dissolved organic complexes and colloidal and particle-bound forms. Some iron species are more readily lost from the euphotic zone by adsorbing onto sinking particles than others. There are indications that colloid aggregation is important as a sink for iron [*Wu and Boyle*, 2002] and is involved in the rapid vanishing of iron in fertilization experiments [*Bowie et al.*, 2001]. Iron speciation therefore possibly determines the residence time of iron in the sunlit surface ocean where it can be used by phytoplankton. Furthermore, not all forms of iron in seawater are equally available for uptake by phytoplankton [e.g., *Hudson and Morel*, 1990; *Maldonado and Price*, 1999, 2001; *Hutchins et al.*, 1999].

[4] A number of recent studies have increased our understanding of many of the processes that influence the speciation of iron, such as organic complexation, photochemical processes, and interactions with colloids and particle surfaces (see section 2.2 for citations). However,

[1] Now at Southampton Oceanography Centre, Southampton, UK.
[2] Now at Marine Sciences Research Center, State University of New York at Stony Brook, Stony Brook, New York, USA.

0886-6236/05/2004GB002340

to understand how speciation influences the residence time and bioavailability of iron in the surface layer of the ocean, the interaction of these individual processes and their linkage to the functioning of the upper-ocean ecosystem has to be studied.

[5] Here we combine what is known about individual processes affecting iron speciation into a comprehensive model of the iron chemistry in the oceanic mixed layer and couple it to a simple ecosystem model. A model similar to our chemical submodel for iron speciation but in coastal waters has been published recently by *Rose and Waite* [2003a]. We apply our model to the site of the Bermuda Atlantic Time-series Study (BATS), an area 85 km south east of Bermuda where a number of physical, chemical, and biological parameters have been measured regularly since 1988 [*Michaels and Knap*, 1996]. The site provides an ideal environment for a first assessment of a comprehensive iron-speciation model because oceanographic conditions and the biogeochemistry are relatively well known. In addition, dust deposition rates [*Kim and Church*, 2001] are available together with some iron concentration profiles [*Wu and Luther*, 1995; *Witter and Luther*, 1998; *Wu et al.*, 2001], which contain speciation information as well. The data provide realistic boundary conditions to the model and allow some comparison of model results with observations and with data-based estimates of iron fluxes at the BATS site [*Jickells*, 1999; *Wu and Boyle*, 2002].

[6] Several of the modeled processes involve parameters that are either not very well known or that have been measured under conditions different from the open-ocean conditions that are considered here. This is, for example, true for iron scavenging and colloid aggregation rates that have both been measured at particle concentrations much higher than those usually observed at the BATS site [*Nyffeler et al.*, 1984; *Wen et al.*, 1997]. Therefore the aim of this study is not to reproduce observations with a single model run, but rather to study the consequences that specific assumptions have for the speciation, concentration, and fluxes of iron at the BATS site, and to test whether these consequences are compatible with the few available observations. At the present stage we see our model primarily as a tool to help in understanding the key processes of the iron cycle and their sensitivities rather than as a numerically accurate reproduction of reality. To this end we therefore investigate the sensitivity of our model outcomes to some less well-known parameter values. Some specific questions are as follows.

[7] 1. How strong is the daily photochemical redox-cycling of iron at the BATS site? How important is the direct photoreduction of iron species compared to the reduction by photoproduced superoxide? Is there an influence of other transition metals on the strength of the redox cycle?

[8] 2. Under which conditions can colloid aggregation lead to a significant loss of iron from the surface layer of the ocean?

[9] 3. How strong is the influence of the solubility and the chemical form of dust-deposited iron?

[10] 4. Does it make a difference to the iron cycle which chemical form of iron is taken up by phytoplankton? How sensitive are model results to changes in the Fe:N or Fe:C-ratio of phytoplankton uptake?

[11] We hope that our investigation of these questions for the BATS location will lead to a better general understanding of iron biogeochemistry and thereby also contribute to studies on much larger spatial and temporal scales [*Johnson et al.*, 1997; *Archer and Johnson*, 1999; *Lefevre and Watson*, 1999; *Christian et al.*, 2002; *Parekh et al.*, 2004]. On these larger scales, the influence of detailed iron speciation can probably be parameterized with simpler models [e.g., *Parekh et al.*, 2004]. A model-based understanding of the role, for example, of colloid aggregation might lead to improvements in these parameterizations. Iron speciation in the mixed layer might also matter for the competition between different phytoplankton groups [*Hutchins et al.*, 1999], and our study therefore hopefully complements studies that have combined a simple iron model with increasingly complex ecosystem models [*Lancelot et al.*, 2000; *Moore et al.*, 2001; *Aumont et al.*, 2003] to address the role of iron in determining phytoplankton species composition. Finally, one outcome of this study is the identification of parameters that need to be better constrained in order to improve the prediction of speciation, concentration, and fluxes of iron in the world ocean.

2. Model Description

[12] In this section we give a brief rationale of the model and an overview of its structure. The model equations are documented in Appendix A.

[13] The model has a chemical and a biological component. The biological model only provides dynamic boundary conditions (e.g., iron uptake by phytoplankton and release during remineralization of organic matter) for the speciation component. Hence, in our modeling approach, phytoplankton growth is not iron limited (which is a reasonable assumption for the BATS site [see *Fung et al.*, 2000; *Watson*, 2003]) and the biological component remains unaffected by the speciation model part.

[14] For simplicity, it is assumed that mixing within the oceanic mixed layer acts on such a short timescale that concentrations within the layer are vertically homogeneous. Model concentrations below the mixed layer are prescribed from observations and influence the concentrations within the mixed layer by turbulent mixing and by entrainment of water during periods of mixed layer deepening.

[15] Model runs start from arbitrary initial conditions and use a combination of observed and modeled time series as external forcing (see below). The integration period is 12 years, of which the first 3 years are spinup. The remaining 9 years cover the period from 1989 until the end of 1997. During spinup the model is driven with a repeated annual cycle of forcing from the year 1989. Already after 1 year of spinup the model reaches a cyclo-stationary state with repeating annual cycles in all variables. A specialized solver for stiff differential equations is used in the integrations.

2.1. Ecosystem Model

[16] The biological part of the model is a nitrogen-based ecosystem model with three compartments, representing

(1) inorganic nitrogen, *N*, which includes nitrate, nitrite, and ammonium, (2) phytoplankton, *P*, and (3) detritus, *D*. The loss of phytoplankton to detritus, representing aggregation and grazing by heterotrophs, is simply modeled as a quadratic function in phytoplankton concentration. We assume linear remineralization and prescribe a constant sinking rate for detritus. We desisted from an explicit representation of zooplankton, since the zooplankton annual cycle itself is hardly constrained from observations and it did not improve the data-model comparison with respect to the other variables. The main effect of that simplification is that the maximum loss of phytoplankton through the quadratic term occurs at the time of the phytoplankton bloom instead of somewhat delayed as would be the case with an explicit representation of zooplankton.

[17] The biological model formulation includes a variable C:N ratio of phytoplankton primary production, depending on the availability of nitrogen and light. This new diagnostic approach greatly improves the modeled carbon uptake under nitrate depleted conditions. The parameterization does not allow for an overall C:N decoupling of the particulate organic matter in the model, but provides a better model counterpart to observed ^{14}C-primary production rates. Models that assume a constant carbon:nitrogen (C:N) stoichiometry in phytoplankton uptake produce systematic errors in carbon fluxes at the BATS site [*Schartau et al.*, 2001; *Schartau and Oschlies*, 2003b], and cannot reproduce the observed maximum rate of carbon uptake shortly after the drawdown in chlorophyll when nitrate becomes depleted. Light adaptation of phytoplankton is represented by a variable chlorophyll:nitrogen ratio, based on work by *Cloern* [1995].

[18] A micro-genetic algorithm of *Carroll* [1996] was applied to minimize the misfit between ecosystem model and observations. The configuration of the algorithm is similar to the one chosen by *Schartau and Oschlies* [2003a]. Here, however, we minimized the misfits between model result observation at the dates of measurement rather than using monthly averages. Particulate organic nitrogen, chlorophyll *a*, ^{14}C-primary production rates, and nitrate concentrations were considered for the assimilation process. Bottle data were extracted of these variables from the BATS web site (http://www.bbsr.edu/cintoo/bats/bats.html). We have processed the data in the following steps: (1) linear interpolation of every bottle cast in the vertical, (2) averaging of the profiles belonging to the same cruise, and (c) averaging this averaged cruise profile vertically over the mixed layer depth (see below for the definition of the mixed layer depth). With the data assimilation procedure, a subset of the biological model parameters (those marked by a superscript in Table 1) was optimized such that the data-model weighted least squares misfit is minimized. The full set of phytoplankton growth parameters cannot be individually constrained [e.g., *Fennel et al.*, 2001] in a 0D-model version. Therefore we assigned a fixed value for the maximum growth rate parameter taken from *Schartau and Oschlies* [2003a]. The optimization yields one best solution of the biological model component which remains unchanged during all subsequent model runs that include the iron chemistry.

[19] The marine ecosystem influences iron chemistry in a number of ways: (1) by uptake of iron during phytoplankton growth and release during remineralization of organic matter; (2) by producing detritus on which iron can be scavenged; (3) by providing a source of organic ligands, either as a byproduct of remineralization or by excretion of siderophores to enhance iron uptake; and (4) by influencing the attenuation of light within the water column and thus photochemical reactions. We assume here that iron is taken up by phytoplankton in constant proportion to either carbon or nitrogen, while the remineralization of iron occurs proportional to that of nitrogen. Iron limitation is unlikely to occur at the BATS site due to large iron input from dust [*Fung et al.*, 2000], so that this assumption may be justified. The iron that is set free during the remineralization of organic matter is assumed to be in organically complexed form.

2.2. Chemical Model

[20] Measurements of iron speciation in seawater are usually reported in terms of operationally defined categories (e.g., by filtration procedures) rather than as chemical speciation in the true sense of the word. To make the model as consistent as possible with such observations, we differentiate between the following five iron species: (1) dissolved inorganic ferric iron Fe(III)′, which includes all hydrolyzed species of $Fe(OH)_n^{3-n}$, (2) dissolved inorganic ferrous iron Fe(II)′, (3) organically complexed iron FeL, (4) colloidal iron Fe_{col}, defined here by filter cutoffs 0.02–0.4 μm [*Wu et al.*, 2001], and (5) iron bound to the surface of sinking particles Fe_p such as dust and organic detritus and aggregated iron (>0.4 μm). The nonreactive part of the particulate iron contained in deposited dust is also modeled, but not further considered here.

[21] A number of processes are known to convert iron in seawater between these forms. The model include the processes of (1) complex formation and dissociation involving organic ligands [*Gledhill and van den Berg*, 1994; *van den Berg*, 1995; *Wu and Luther*, 1995; *Rue and Bruland*, 1995; *Witter and Luther*, 1998; *Witter et al.*, 2000; *Rose and Waite*, 2003c]; (2) photoreduction of the different iron forms, both directly [*Wells and Mayer*, 1991; *Kuma et al.*, 1992; *Johnson et al.*, 1994; *Barbeau and Moffett*, 2000; *Barbeau et al.*, 2001; *Emmenegger et al.*, 2001; *Barbeau et al.*, 2003], and indirectly by photoproduced superoxide [*Voelker and Sedlak*, 1995; *Miller et al.*, 1995]; (3) oxidation of Fe(II)′ by oxygen, superoxide, and hydrogen peroxide [*Millero et al.*, 1987; *Millero and Sotolongo*, 1989; *King et al.*, 1995]; (4) scavenging onto sinking particles [*Balistieri et al.*, 1981; *Nyffeler et al.*, 1984; *Johnson et al.*, 1997]; (5) colloid formation [*Johnson et al.*, 1994; *Rose and Waite*, 2003b]; and (6) aggregation of colloids [*Wells and Goldberg*, 1993; *Wen et al.*, 1997]. Rate laws and constants for these processes were taken from the indicated literature. To represent the kinetics of interconversion between the different forms of iron, we also model the concentrations of free iron-binding organic ligands [L], of hydrogen peroxide [H_2O_2], of superoxide [O_2^-], and of sinking particles, both inorganic from dust deposition, and organic detritus (see Appendix A). A sketch of the iron pools and fluxes between them is shown in Figure 1. For

Table 1. Standard Model Parameters

Parameter	Symbol	Unit	Value
	Chemistry		
Fe(II)′ oxidation rate by O_2	k_{ox1}	$\mu M^{-1}\ d^{-1}$	0.864
Oxygen concentration	$[O_2]$	μM	214
Fe(II)′ oxidation rate by O_2^-	k_{ox2}	$nM^{-1}\ d^{-1}$	864
Fe(II)′ oxidation rate by H_2O_2	k_{ox3}	$nM^{-1}\ d^{-1}$	6.24
Fe_{col} photoreduction rate at 30 $\mu E\ m^{-3}\ s^{-1}$	k_{ph1}	d^{-1}	20.2
FeL photoreduction rate at 30 $\mu E\ m^{-3}\ s^{-1}$	k_{ph2}	d^{-1}	86.4
Fe(III)′ photoreduction rate at 30 $\mu E\ m^{-3}\ s^{-1}$	k_{ph3}	d^{-1}	1.32
Fe_p photoreduction rate at 30 $\mu E\ m^{-3}\ s^{-1}$	k_{ph4}	d^{-1}	20.2
Fe_{col} formation rate	k_{col}	d^{-1}	2.4
FeL formation rate	k_{fel}	$nM^{-1}\ d^{-1}$	172.8
FeL dissociation rate	k_{ld}	d^{-1}	8.64
Fe(III)′ reduction rate by O_2^-	k_{red}	$nM^{-1}\ d^{-1}$	1.3×10^4
Fe(III)′ scavenging rate	k_{sca}	$kg^{-1}\ l\ d^{-1}$	2.5×10^4
Fe_{col} aggregation rate	k_{ag}	$kg^{-1}\ l\ d^{-1}$	1.224×10^6
O_2^- dismutation rate	k_{dm}	$nM^{-1}\ d^{-1}$	2.64
O_2^- production rate at 30 $\mu E\ m^{-3}\ s^{-1}$	$S_{O_2^-}$	$nM\ d^{-1}$	1037
H_2O_2 decay rate	k_{dis}	d^{-1}	0.24
	Biology		
Maximum growth rate at 0°C	μ^*	d^{-1}	0.27
Phytoplankton mortality at 0°C	ρ_P	d^{-1}	0.005[a]
Initial slope P-I curve	α	$m^2\ W^{-1}\ d^{-1}$	0.159[a]
Nitrate half-saturation constant	K_N	μM	0.68[a]
Phytoplankton aggregation rate	Φ^*_P	$\mu M^{-1}\ d^{-1}$	0.64[a]
Detritus remineralization rate at 0°C	γ_D	d^{-1}	0.02[a]
Coefficient for temperature function	C_{ref}	-	1.066
PAR:short-wave irradiance ratio	f_{PAR}		0.43
Attenuation due to water	k_w	m^{-1}	0.04
Attenuation due to chlorophyll	κ	$(mg\ Chl)^{-1}\ L\ m^{-1}$	0.01[a]
Minimum C:N ratio	Q_{min}	-	5.4
Maximum C:N ratio	Q_{max}	-	22
Slope parameter for C:N ratio	σ	-	0.48[a]
Fe:N ratio in organic matter	$r_{Fe:N}$	$nM\ \mu M^{-1}$	3.31×10^{-2}
Mass:N ratio in organic matter	$r_{m:N}$	$g\ mol^{-1}$	159
	Physics		
Mixing rate	k_{mr}	$m\ d^{-1}$	1.15[a]
Sinking velocity	w_s	$m\ d^{-1}$	18

[a]Parameter values that were optimized in the data assimilation (section 2.1).

each of the model species, a mass balance equation is solved that takes into account the listed reactions plus sources and sinks from atmospheric deposition, sinking, and mixing of waters at the base of the mixed layer.

2.3. Forcing

[22] Several processes in the model depend on external forcing. Solar irradiance as well as the depth and temperature of the oceanic mixed layer influence the growth rate of phytoplankton. In addition, irradiance drives photochemical reactions. Dust deposition is a source of inorganic sinking particles and iron, and precipitation is a source of hydrogen peroxide.

[23] We used time series of precipitation and daily averaged irradiance for the BATS location by *Doney* [1996]. Precipitation is low, around 3.7 mm day^{-1} in the mean, and has no pronounced annual cycle. Daily averaged irradiance varies between 80 W m^{-2} in winter and 300 W m^{-2} in summer. A daily cycle of irradiance was constructed from the daily averaged values using standard astronomical formulae for daylength and zenith angle [*Brock*, 1981].

[24] Vertical profiles of temperature and salinity from the approximately biweekly BATS cruises are available since October 1988. We constructed a time series of mixed layer depth and temperature directly from BATS CTD data (http://www.bbsr.edu/cintoo/bats/bats.html), defining the lower boundary of the mixed layer by the depth at which temperature is 0.1° colder than at the surface. If more than one CTD cast was available within a cruise, we averaged the temperature profiles before calculating the mixed layer depth. The annual mixed layer cycle is characterized by a maximum depth between 150 and 350 m that is usually attained at the end of the winter, followed by a rapid shoaling toward the summer, where mixed layer depths are around 20 m. The mixed layer typically begins to deepen again in September.

[25] Daily values of dust deposition (both wet and dry) at the BATS site were taken from the output of a global atmospheric dust transport model [*Mahowald et al.*, 1999]. The average dust deposition between 1989 and 1998 at the nearest model grid point to the BATS location is 2.3 mg $m^{-2}\ d^{-1}$. Most of that deposition occurs in June to September (average 5.3 mg $m^{-2}\ d^{-1}$ in that period), reflecting the arrival of dust blown off the Sahara, while the average deposition is low in the remaining months. This annual pattern and the average value agree well with

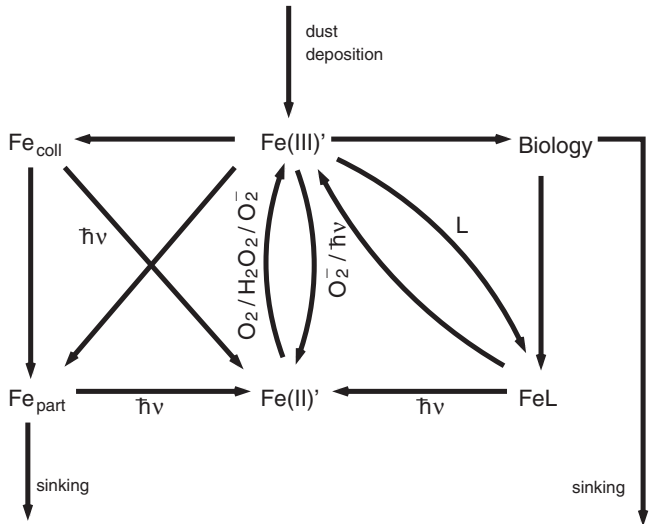

Figure 1. Schematic representation of the iron pools represented in the model and the fluxes between them. Photochemically driven processes are marked with $h\nu$. The fluxes due to mixing and entrainment at the base of the mixed layer are not shown.

observational values for dust deposition at Bermuda between September 1996 to September 1997 by *Kim et al.* [1999]. There is considerable day-to-day variability in the dust deposition, with frequent changes over 2 orders of magnitude from one day to the next. Annually averaged dust deposition varies between 1.3 (1997) and 3.4 (1985) mg m^{-2} d^{-1}.

[26] To convert dust deposition to iron flux, we assumed that the deposited dust has a composition close to that of average crustal material, with a weight percentage of 3.5% of iron [*Duce and Tindale*, 1991], and that a fixed fraction of that iron is dissolvable after deposition to the sea surface [*Jickells*, 1995]. The nonreactive part of the iron contained in dust is not further considered here.

3. Results and Discussion

3.1. Ecosystem Model

[27] The optimized ecosystem model yields best results for chlorophyll a concentration (Figure 2c) and carbon-based primary production (Figure 2d). Limitations in modeled PON dynamics (Figure 2b) are detectable and may result from the simplifications of the NPD model, for example the neglect of zooplankton and bacteria biomass. Focusing on the simulated concentrations of dissolved inorganic nitrogen (DIN, actually representing nitrate, nitrite, and ammonium), we find winter values close to observations with some distinct interannual variations (Figure 2a). The modeled summer DIN concentrations are somewhat higher than the observed nitrate concentrations by about 0.1 mmol N m^{-3}. However, this deficit falls within the range of the analytic detection limit and the data-model intercomparison uncertainty, since ammonium observations were not explicitly regarded. The few available ammonium measurements are close to this summer deficit.

[28] Simple nitrogen-based ecosystem models generally underestimate primary production shortly after the bloom period and during summer [*Schartau et al.*, 2001; *Schartau and Oschlies*, 2003b]. Our model uses a very simple parameterization of the C:N uptake ratio of phytoplankton that basically increases under nitrogen limitation and therefore emulates some of the dynamics as it is expressed in more complex models where C and N utilization are fully decoupled [e.g., *Geider et al.*, 1998; *Bissett et al.*, 1999; *Mongin et al.*, 2003]. Since the C:N decoupling is so important under oligotrophic conditions, this particular parameterization allows the model to capture the annual cycle and interannual variability of PP very well, in spite of the fact that it is only nitrogen based. The modeled carbon uptake rate provides an important link to the chemical iron speciation component, especially when a constant Fe:C ratio is assumed rather than a fixed Fe:N uptake rate.

[29] Estimates of the annual export production or new production at the BATS site range from 0.7 mol C m^{-2} to 4.4 mol C m^{-2}, depending on the method used [*Carlson et al.*, 1994]. Our model predicts an annual export of 3.4 mol C m^{-2} out of the mixed layer by mixing, detrainment, and sinking of particulate organic matter, assuming a constant Redfield N:C ratio in particulate organic matter. Using the sinking and remineralization rate from the model, a scaling of the export to a depth of 150 m results in 2.5 mol C m^{-2}, somewhat higher than the trap-based estimates at that depth cited by *Carlson et al.* [1994] (0.7 mol C m^{-2}). Part of that discrepancy might be explained by the absence of a dissolved organic matter pool in our model.

[30] In general the model results show a passable fit to the observations, comparable to results of more complex models, such as those of *Hurtt and Armstrong* [1996] and *Spitz et al.* [2001], although it does not include an explicit representation of zooplankton, bacteria, ammonia, or dissolved inorganic carbon. Further improvement in the biological model would probably require making the C:N ratio not only in the uptake, but also in the particulate biomass variable. A second improvement would be the resolution of the depth-dependency to avoid the unphysical prescription of deep nitrate concentration.

3.2. Particulate Material

[31] In the open ocean, most of the particles within the surface mixed layer are usually of biological origin. *Jickells et al.* [1990] showed that at the BATS site, more than 60% of the particulate matter in the upper 200 m of the water column are organic, while less than 5% are terrigeneous clays. The rest is presumably mainly calcite and silicate shells of planktonic organisms. However, episodic dust deposition events might increase concentrations of terrigeneous particles temporarily, leading to enhanced scavenging and thus loss of iron. In the model, sinking particles are therefore split into two classes, one representing detritus, the other representing deposited terrigeneous material. For simplicity, we have assumed an equal sinking rate for both. The concentration of detritus (in kg L^{-1}) is calculated from the nitrogen-based ecosystem model, assuming a fixed Redfield C:N stoichiometry and that half of the mass of

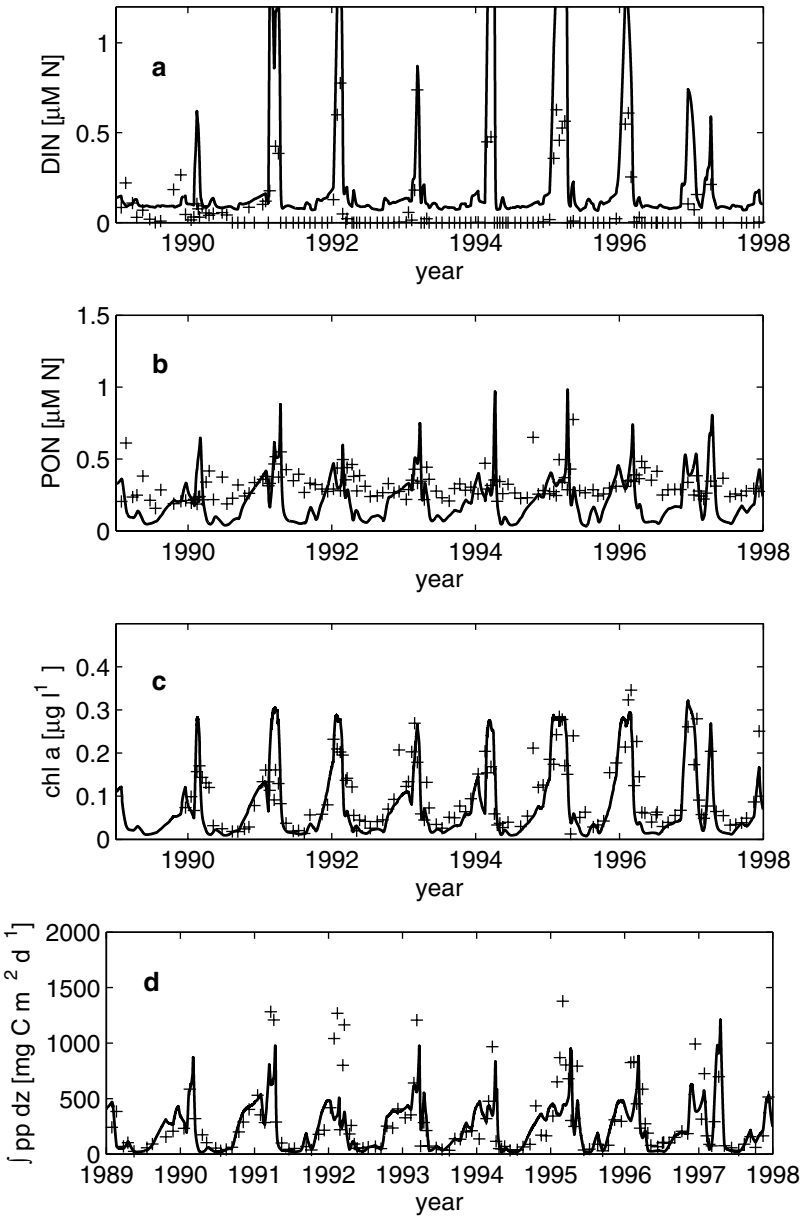

Figure 2. Observed (crosses) and modeled (line) concentrations (a) of nitrate + nitrite, (b) of particulate organic nitrogen, and (c) of chlorophyll, and (d) vertically integrated primary productivity at the Bermuda Atlantic Time-series Study (BATS) site. Observations have been averaged for each cruise and over the mixed layer depth, as described in section 2.3.

detritus is carbon. Scavenging of iron depends on particle surface area rather than mass. To keep the model simple we assume that the two are proportional, i.e., that the particle size spectrum is invariant.

[32] Under these assumptions, model results show a strong dominance of biological versus terrigeneous particles over most of the year. Only in late summer, when dust deposition reaches its peak, inorganic particles are more abundant than detritus. On average, the concentration of biogenic particles is about 2 orders of magnitude larger than that of inorganic particles. The average composition and annual cycle of particles are broadly consistent with *Jickells et al.* [1990]. The modeled total concentration of particles is significantly lower (12 mg m^{-3}) than the value by *Jickells et al.* [1990] (55 mg m^{-3}). This difference is due to (1) silicate and calcite shells which are not represented in our model and to (2) the underestimation of particulate organic nitrogen by the model (Figure 2b). We therefore conclude that the model is likely to underestimate scavenging of iron onto sinking particles somewhat, although a larger source of uncertainty is probably the scavenging rate.

3.3. Reactive Oxygen Species

[33] The redox state of dissolved iron in the ocean is strongly influenced by the two reactive oxygen species

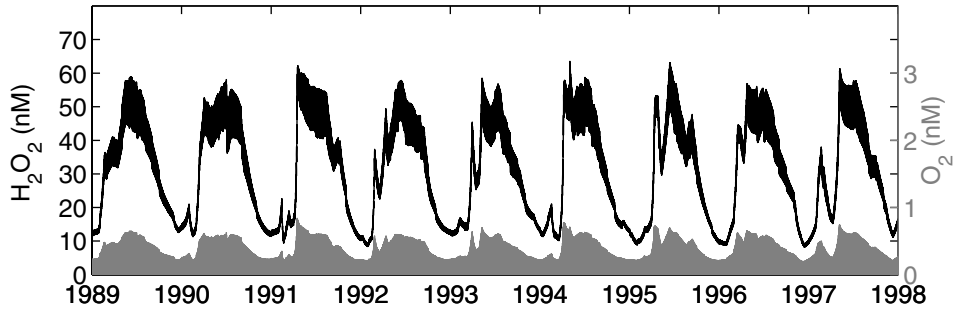

Figure 3. Modeled concentrations of hydrogen peroxide (black), and of superoxide (shaded). Note the different scale for the two concentrations.

superoxide, O_2^-, and hydrogen peroxide, $H_2\ O_2$. Both species are strong oxidants for Fe(II)′, but O_2^- also acts as a strong reductant for Fe(III)′.

[34] The dominant source of reactive oxygen species in seawater is the photo-oxidation of colored dissolved organic matter (CDOM) [*Cooper et al.*, 1988] that produces superoxide, and the subsequent transformation of superoxide to hydrogen peroxide. The latter transformation can proceed directly by the reaction of two superoxide molecules to hydrogen peroxide (dismutation) or catalyzed by the reduction and subsequent oxidation of a Fe(III) ion. Both processes consume two molecules of superoxide, and produce one molecule of hydrogen peroxide,

$$2O_2^- \rightarrow H_2O_2 + O_2 + 2OH^-, \quad (1)$$

$$\begin{aligned} \mathrm{Fe(III)}' + 2O_2^- &\rightarrow \mathrm{Fe(II)}' + O_2 + O_2^-, \\ &\rightarrow \mathrm{Fe(III)}' + O_2 + H_2O_2 + 2OH^-. \end{aligned} \quad (2)$$

Our model does not include an explicit CDOM pool, so we assume the photoproduction rate of superoxide to be proportional to light intensity. *Voelker and Sedlak* [1995] give a range of O_2^- photoproduction rates in midday sunlight between 3 and 300 pmol $L^{-1}\ s^{-1}$ in oligotrophic and productive surface waters, respectively. In our model solutions, $[H_2O_2]$ varies approximately linearly with the photoproduction rate. We choose a rate of 12 pmol $L^{-1}\ s^{-1}$ in our standard experiment, because with that rate the model produces summer mixed layer $[H_2O_2]$ values around 50 nmol L^{-1}, close to observations in the subtropical Atlantic [*Obernosterer et al.*, 2001].

[35] Rain events can lead to significant increases in $[H_2O_2]$ in seawater [*Kieber et al.*, 2001]. Here monthly averaged precipitation rates are used, and therefore such singular events are not reproduced. We find that over longer timescales, rainfall and the uncatalyzed dismutation (equation (1)) are of minor importance as a source of H_2O_2, compared to the iron-mediated conversion of superoxide (equation (2)).

[36] The modeled concentrations of H_2O_2 and O_2^- are shown in Figure 3. The lifetime of superoxide is extremely short, so that its concentration during the night is essentially zero. The maximum concentration reached at noon shows an annual cycle that reflects the annual cycle of irradiance (see discussion in section 2.3). The model produces maximum values of up to 0.7 nM in summer, when the mixed layer is shallow and the irradiance at the sea surface is highest, and around 0.2 nM in late winter.

[37] The mixed-layer averaged concentration of H_2O_2 in the model shows a strong annual cycle, varying between about 10 nM in winter and around 60 nM in summer. This annual cycle is overlaid by a daily cycle with a 1 nM amplitude in winter and about 10 nM in summer. The amplitude of the daily cycle in summer is similar to observed amplitudes in waters of the open tropical and subtropical Atlantic [*Yuan and Shiller*, 2001; *Obernosterer et al.*, 2001].

[38] The timescale for concentration changes of the reactive oxygen species is similar to that of vertical mixing, so that vertical gradients in these species might persist for some time within the mixed layer [*Doney et al.*, 1995], contrary to the assumptions in our model. Owing to the nonlinearities in the chemical reaction equations, this might lead to a daily cycle of the vertically averaged concentrations that differs by some degree from the predictions of our vertically averaged model. Mainly in winter, when the mixed layer is deep, we assume a stronger daily cycle at the surface than the one predicted with our zero-dimensional model. However, we do not expect the deviations to be very large since the timescales are similar.

3.4. Diurnal Variability of Iron Speciation

[39] The modeled iron speciation shows a strong diurnal variability, especially in summer (Figure 4). During the night, FeL and Fe_{col} are the dominant forms of iron. After sunrise their concentrations decrease quickly while that of Fe(II)′ increases. A few hours after noon, [Fe(II)′] reaches its maximum and decreases afterward while [Fe(III)′] increases.

[40] Because of its short lifetime in oxygenated seawater, there must be a well-sustained source of Fe(II)′ throughout the day. Fe(II)′ is produced by direct photoreduction of ferric iron species, and by the reduction of Fe(III)′ by photoproduced superoxide. In our model results, the last process, the reduction by superoxide, operates at a rate that is up to more than a hundred times the maximum rate of all direct photoreductive processes taken together. The dominance of reduction by superoxide over direct photoreduction has already been proposed for a simpler laboratory system by *Voelker and Sedlak* [1995].

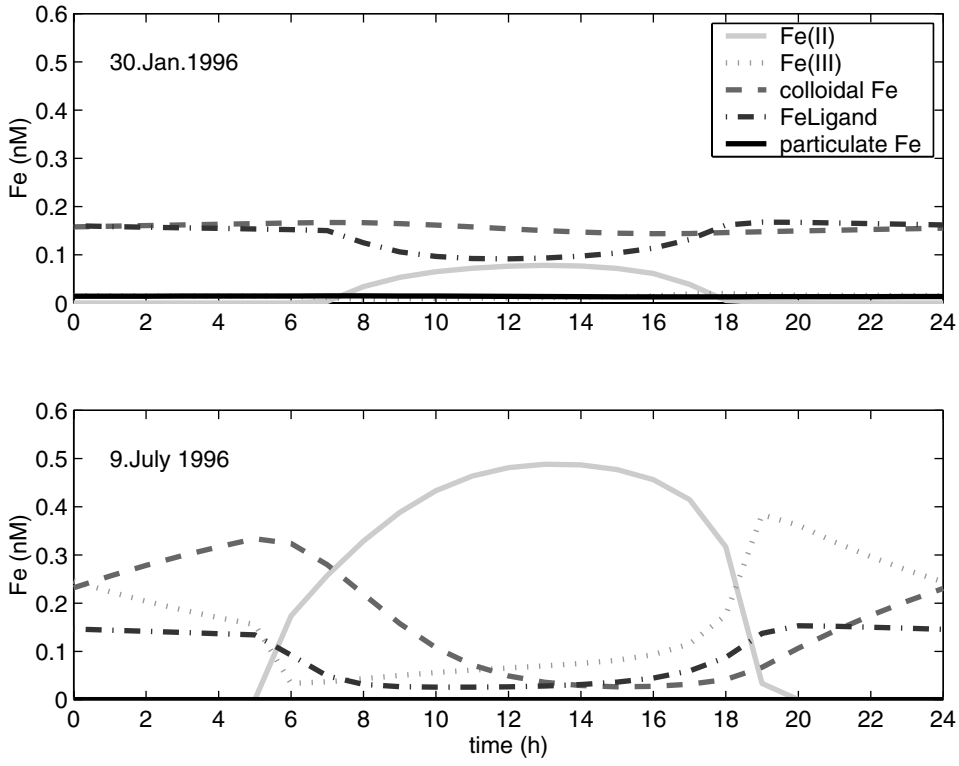

Figure 4. Modeled concentrations of iron species. (top) Daily variability in winter. (bottom) Daily variability in summer.

[41] The produced Fe(II)′ is subsequently oxidized again to Fe(III)′ by O_2, O_2^-, and H_2O_2. The strong diurnal cycle of $[H_2O_2]$ and $[O_2^-]$ (Figure 3) leads to a corresponding cycle of the redox-reactions. Until midday, iron reduction outweighs the oxidation, leading to an increase of [Fe(II)′], but also of [Fe(III)′] at the expense of $[Fe_{col}]$ and [FeL]. In the afternoon the balance between reduction and oxidation is reversed because $[H_2\ O_2]$ reaches its maximum, and [Fe(II)′] decreases. During the night all photochemical reactions stop so that all Fe(II)′ is oxidized to Fe(III)′. Parts of Fe(III)′ are quickly complexed by free organic ligands, with rates up to 5.3 nM d^{-1}. The formation of colloidal iron is a much slower process (up to 1.1 nM d^{-1}) compared to organic complexation and oxidation, so that $[Fe_{col}]$ increases slowly at the cost of [Fe(III)′] during the night.

[42] In summer, the modeled total iron concentration becomes larger than the complexation capacity by organic ligands (see Figure 6 in section 3.5), leading to enhanced formation of colloidal iron during the night. See sections 3.5 and 4.6 for discussion.

[43] The diurnal cycle of iron speciation at the BATS site is much weaker in winter than in summer (Figures 4 and 5) due to a combination of less sea surface irradiance, deeper mixed layers, and higher attenuation by chlorophyll that all reduce the vertically averaged irradiance within the mixed layer in winter.

[44] There is only limited data available to validate the modeled daily cycle in iron speciation. Measurements of the organic complexation of iron [*Wu and Luther*, 1995; *Wu et al.*, 2001; *Witter and Luther*, 1998] and of colloidal iron [*Wu et al.*, 2001] take substantial time after sampling. They therefore most likely reflect near-equilibrium conditions with no or little photochemical production of Fe(II)′ that can best be compared with model results of the night. The modeled average nighttime concentration of colloidal iron in July is 0.24 nM, somewhat smaller than the observation at the BATS site by *Wu et al.* [2001] (0.47 nM).

[45] Measurements of [Fe(II)′] in the ocean are still relatively rare [*O'Sullivan et al.*, 1991; *Kuma et al.*, 1992; *Waite et al.*, 1995; *Croot et al.*, 2001], but generally have shown nonvanishing values of [Fe(II)′]. *Waite et al.* [1995] have observed a speciation cycle of comparable strength to our model results in Australian shelf waters, a system with much higher concentrations of organics and total iron than for open ocean conditions. The concentrations observed in the Southern Ocean by *Croot et al.* [2001] are of a similar order of magnitude as our model results. We are currently unaware of any [Fe(II)′] measurements at the BATS location. In the absence of more speciation data we therefore cannot come to a final conclusion yet whether the strength of the modeled daily cycle of [Fe(II)′] is realistic, but we can discuss its dependency on assumptions in the model.

[46] The main factor that influences values of [Fe(II)′] is its production rate either by direct photoreduction of ferric iron species, especially of FeL, or by reaction with O_2^-. Although the direct photoreactivity of ferric iron species may be lower than assumed here [*Barbeau et al.*, 2003], this is unlikely to affect [Fe(II)′] significantly. The reduction of

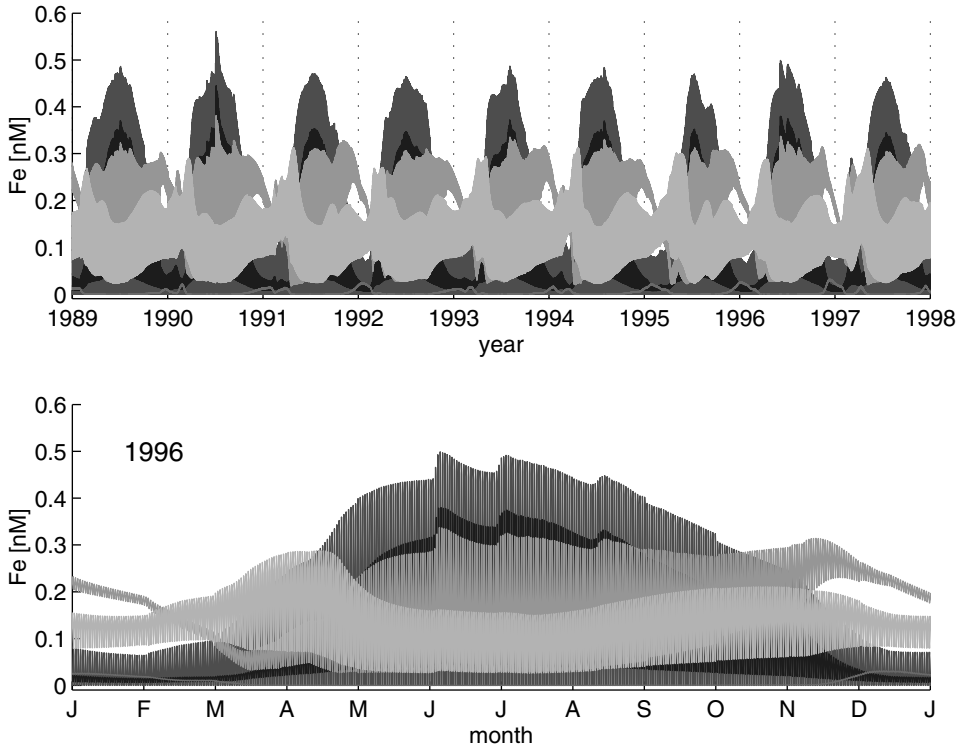

Figure 5. Modeled iron speciation ([Fe(III)′], blue, [Fe(II)′], red; [Fe_{col}], green; [FeL], cyan; [Fe_p], purple). (top) Interannual variability. (bottom) Annual variability (year 1996). See color version of this figure at back of this issue.

Fe(III)′ by O_2^- dominates. The main uncertainty is therefore the value of [O_2^-] that has to our knowledge not been measured so far at the BATS site.

[47] We have constrained the photoproduction rate of O_2^- by demanding the modeled values of [H_2O_2] to be close to observed values. Constraining [O_2^-] with [H_2O_2], however, works only if the model includes all significant sinks of O_2^-. *Voelker and Sedlak* [1995] have shown that reaction 2 can also be catalyzed by copper, a reaction that has not been included in the present model run. The possible influence of copper is considered further in section 4.5. In reality, one might also expect that the speciation cycle is somewhat stronger close to the surface and weaker at the base of the mixed layer (section 3.3).

3.5. Annual Cycle and Interannual Variability of Dissolved Iron

[48] The modeled total concentration of dissolved and colloidal iron ([Fe_T] = [Fe(III)′] + [Fe(II)′] + [FeL] + [Fe_{col}]) changes between 0.3 nM in spring and 0.7 nM in summer (Figure 6). Our results are close to observed values in summer (0.6 nM in July 1992 [*Wu and Luther*, 1994] and 0.58 nM in July 1998 [*Wu and Boyle*, 2002]) but higher than observations in spring (0.2 in March 1998 [*Wu and Boyle*, 2002]) and in autumn (0.2 nM in October 1991 [*Wu and Luther*, 1994]). Two mechanisms that could explain the difference are considered in sections 4.2 and 4.4. *Wu and Boyle* [1998] also measured around 0.5 nM Fe in surface water near Bermuda.

[49] The total concentration of organic ligands ([L_T] = [L] + [FeL]) varies between 0.15 nM in summer and about 0.5 nM to 0.85 nM in late winter/early spring (Figure 6). This annual cycle results from the influence of the annual cycle of mixed layer depth and from the concentration of total organic ligands below the mixed layer. The latter was prescribed using a linear fit to observations of soluble ligands in the eastern North Atlantic from *Wu et al.* [2001]. The annual variation is somewhat stronger than the range of observations by *Wu and Luther* [1995] (0.3 nM to 0.6 nM) which, however, do not necessarily cover the complete seasonal variability. The modeled excess of total ligand over iron in summer has no counterpart in observations at the BATS location. This is clearly an indication that our model is too simplistic with respect to organic ligands and that probably a production of ligand by the biota has to be included in future models. Here we restrict ourselves to studying the effect of a persistent ligand excess on the cycling of iron (section 4.6). The temporal variation of [Fe_T] in the mixed layer is caused by seasonal variations in biological uptake and remineralization, scavenging, dust deposition, and exchange with deeper water (Figure 7a).

[50] The spring phytoplankton bloom leads to a strong uptake of iron. Only part of the iron taken up is remineralized, so that a significant drawdown of iron is observed. During spring the drawdown of iron is further enhanced by the formation of detritus that leads to increased scavenging of iron on particles. Most of the scavenging flux (99.7%

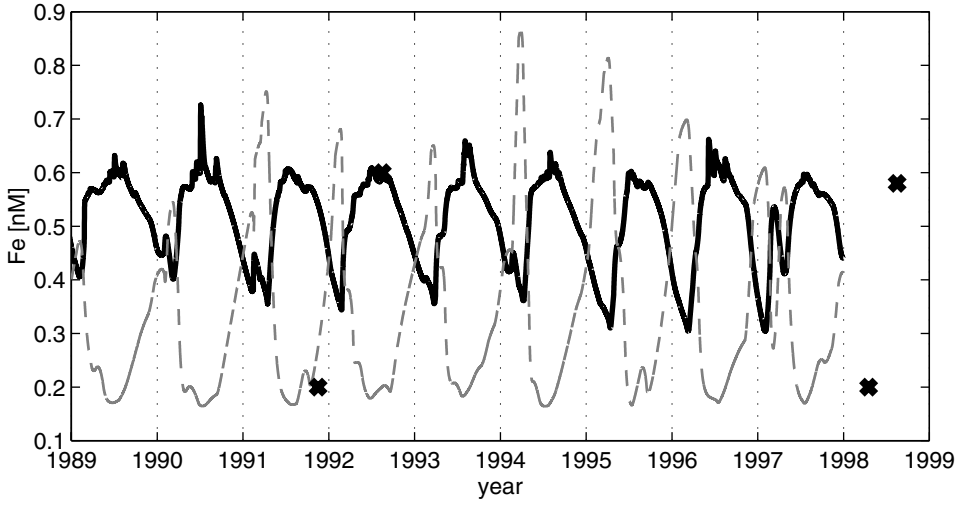

Figure 6. Modeled total Fe (solid black line) and total ligand concentration (dashed shaded line) as well as observed iron concentration by *Wu and Luther* [1994] and *Wu and Boyle* [2002] (crosses).

in the annual mean) occurs through colloid aggregation, only 0.3% through direct scavenging from the dissolved phase.

[51] In summer the dust deposition reaches its annual maximum. At the same time the mixed layer is very shallow so that the incoming iron is distributed over a lower depth than during the rest of the year. Since biological productivity is low, the dust deposition results in an elevated iron concentration.

[52] The flux of iron due to the exchange with water from below the mixed layer changes direction during the year (see Figure 7a). The main export and import processes by water exchange are caused by the annual cycle of the mixed layer depth. During the deepening of the mixed layer at the

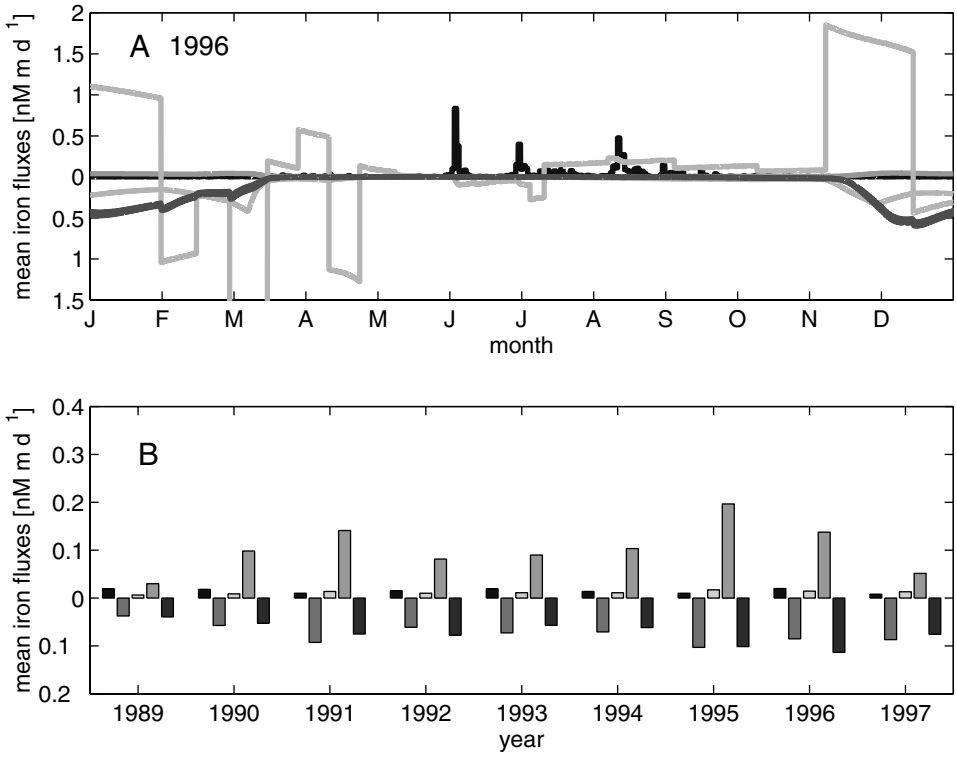

Figure 7. Modeled iron fluxes (dust deposition, blue; biological uptake, light blue; remineralization of biological matter, green; exchange with deeper water, orange; scavenging, brown). See color version of this figure at back of this issue.

Table 2. Comparison of Iron Flux Estimates at the BATS Site With Average Fluxes From the Model[a]

Iron Flux	*Jickells* [1999]	Model Average (1989–1998)
Dissolved atmospheric input	100	15
Biological export	−4–−105	−51
"Upwelling" flux	3–40	106
Scavenging loss	n.a.	−72

[a]Iron flux estimates at the BATS site are taken from *Jickells* [1999]. All fluxes are given in 10^{-3} μmol m^2 d^{-1}, and positive values are into the mixed layer. Here n.a. denotes "not applicable."

end of the year, water from below is mixed in and delivers new iron. Owing to the mixed layer shoaling in spring, iron is lost to deeper water. The annual input by entrainment of water during mixed layer deepening is higher than the export during mixed layer shoaling, because the strongest annual mixed layer shoaling takes place during the plankton bloom when iron concentrations within the mixed layer are low.

[53] A further process of water exchange is the permanent turbulent mixing at the base of the mixed layer. Since the total concentration of dissolved and colloidal iron is mostly lower within the mixed layer than below, it leads to a net upward transport of iron, albeit only half as strong as the annual mixed layer cycle.

[54] The different iron fluxes are also very variable on interannual scales (see Figure 7b). Lower iron input and/or higher biological export of different years are compensated by water mass mixing. In years with low atmospheric deposition or high biological export, less iron can be exported by mixing with deeper water so that the import due to water mixing is relatively high, since the net import is equal to import minus the export. This ensures that the interannual cycle of the iron concentration is stable and barely dependent on the strength of the biological activity and atmospheric deposition.

[55] *Jickells* [1999] estimated a budget of the various iron fluxes at the BATS site from available observations. A comparison of his estimate with our average budget (Table 2) displays some similarities but also some differences. His estimate of dissolved iron input from dust is about 7 times higher than ours, due to a combination of a higher estimate of total iron input (4.2 μmol m^{-2} d^{-1}, versus 1.4 μmol m^{-2} d^{-1}) and higher average solubility (2.4% versus 1%). Both flux values are possible; see section 4.1. Our average net biological iron uptake falls within the (fairly broad) range given by *Jickells* [1999]. However, we obtain a much stronger vertical flux from mixed layer dynamics than his estimate of the vertical diffusion. This can be explained by the fact that our fluxes involve the temporal correlation of mixed layer depth and iron concentration, an effect that cannot be captured by estimating the flux from vertical diffusivity and an average concentration profile. In fact, our vertical flux from turbulent mixing at the base of the mixed layer is within the range given by *Jickells* [1999]. In our budget, the large upward flux of iron from mixed layer dynamics is to a large part compensated by the sinking of iron scavenged onto particles, a process that *Jickells* [1999] has not attempted to estimate. We would like to emphasize here that we do not consider our budget in any way more realistic than the one by *Jickells* [1999] given the large uncertainty in the parameter values that we have used. However, it demonstrates the importance of mixed layer dynamics when considering the balance of fluxes at the BATS site.

4. Sensitivity Studies

[56] Current research is bringing the iron biogeochemistry into a sharper focus, but uncertainties remain in critical parts of the iron system. To date, the aim of our iron model is not so much to give accurate numerical predictions of iron fluxes and concentrations, but to provide a numerical modeling environment, which allows to better investigate the complex relation between iron inputs, speciation, and bioavailability in oceanic surface waters. The differentiation between the various forms of iron allows us to have a closer look at single processes of the complex biogeochemistry of the iron cycle and enables us to make statements about how sensitive model results are to changes in less well-constrained parameter values.

4.1. Solubility of Atmospheric Iron

[57] The solubility of iron in deposited dust depends on the form of deposition (wet or dry), the composition, and the atmospheric history (e.g., the number and duration of times the dust particle underwent entrapping in water droplets and subsequent drying) of the dust particle [*Spokes and Jickells*, 1996; *Jickells and Spokes*, 2001; *Arimoto*, 2001]. Observed solubilities vary between 0.1 and 10%, with earlier measurements or estimates [*Zhuang et al.*, 1990; *Duce and Tindale*, 1991] generally tending toward higher values than more recent ones [*Spokes and Jickells*, 1996; *Jickells and Spokes*, 2001]. This large range of solubilities means that iron fluxes that are calculated from model-based [*Mahowald et al.*, 1999] or observation-based [*Kim et al.*, 1999; *Kim and Church*, 2001] dust deposition rates have an uncertainty of at worst 2 orders of magnitude. It is therefore crucial to study the sensitivity of the modeled iron concentrations and fluxes to variations in this parameter.

[58] We conducted several model runs which differ only in the solubility (between 0.1 and 10%) of iron from dust. The variation of solubility over 2 orders of magnitude does not lead to a proportional variation of the concentration of total dissolved iron within the mixed layer (Figure 8). On average, the concentration is 1.2 times (maximally 3 times) higher for the model run with 10% solubility, compared to the model run with 1% solubility. Most affected are the summer concentrations, when the stable and shallow mixed layer prevents exchange with deeper waters. Increasing the solubility above 2.5% leads to summer values of $[Fe_T]$ over 1 nM which are incompatible with observations.

[59] Why are the mixed layer concentrations so insensitive to the value of the solubility? Over annual timescales, the input of iron from dust deposition must be balanced by other fluxes of iron into or out of the mixed layer. The three other fluxes are (1) net biological uptake, (2) loss of iron adsorbed to the surface of sinking particles, and (3) exchange with

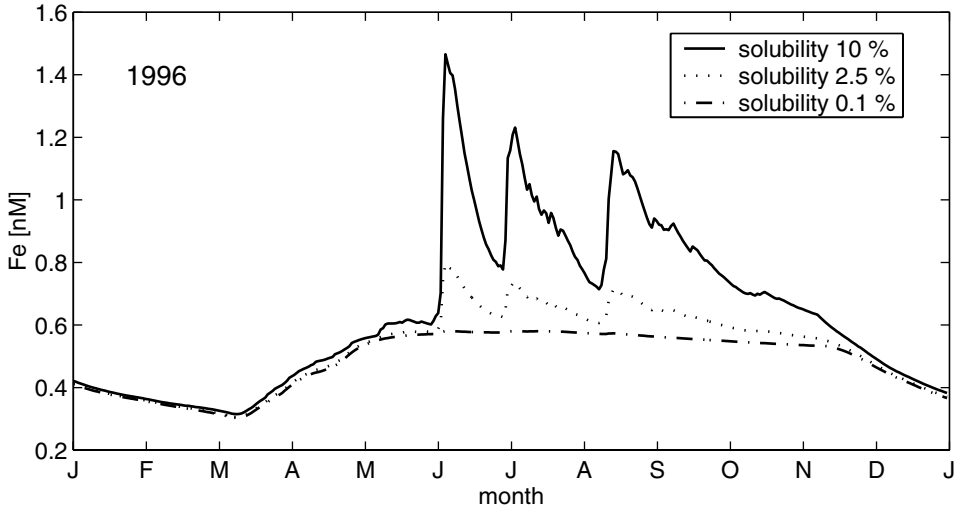

Figure 8. Total Fe concentration of model runs with varying solubility of deposited dust (year 1996).

water below the mixed layer by turbulent mixing, entrainment and detrainment. The biological uptake (flux 1) is fixed, as we have assumed a fixed phytoplankton Fe:N ratio and a growth rate independent of Fe concentrations.

[60] Compensation by sinking of iron adsorbed on particles (flux 2) is possible if more iron is adsorbed per particle. The two pathways of adsorption are scavenging and aggregation of colloids. Both pathways involve a step whose rate is proportional to [Fe(III)′]. A 10 times higher loss by flux 2 would thus imply a 10 times higher concentration of [Fe(III)′] with unchanged concentration of particles. This is not found in our model results.

[61] The main process that damps changes of [Fe_T] with varying iron input is the mixing with deeper water (flux 3). The mean annual flux of iron due to exchange with deeper water is the difference of a strong positive flux during mixed layer deepening and a negative flux during mixed layer shoaling (Figure 7 and section 3.5). The import flux is proportional to below the mixed layer, while the export flux is proportional to [Fe_T] within the layer. Because the net flux is the difference between two large opposite fluxes, a small change in [Fe_T] within the mixed layer can lead to a large change in the export flux and hence in the net flux.

[62] The weak sensitivity of iron concentrations to the solubility is therefore caused by the strong vertical mixing mainly associated with the annual mixed layer cycle at the BATS site. Similar behavior would be expected at other locations with strong vertical mixing, but not at more stratified oceanic regions, for example, in the tropics.

4.2. Fe:N and Fe:C Ratio of the Phytoplankton Uptake

[63] The uptake of iron is modeled assuming either a constant Fe:N ratio or a constant Fe:C ratio in phytoplankton primary production. Observed Fe:N- or Fe:C-ratios of different phytoplankton species vary over up to 2 orders of magnitude: *Sunda and Huntsman* [1995, 1997] reported Fe:C-ratios between 2 and 13 μmol mol^{-1} (Fe:N 13–86 μmol mol^{-1}, assuming Redfield stoichiometry) for open ocean phytoplankton, and much higher values for coastal species, while *Muggli et al.* [1996] measured a comparatively high Fe:N ratio of 250 μmol mol^{-1} in an open ocean diatom. Moreover, phytoplankton cells seem to possess the physiological plasticity to adapt their Fe:C-ratio to environmental conditions, such as iron limitation [*Sunda and Huntsman*, 1995].

[64] In the standard model run, we assume an Fe:N-ratio of 33 μmol mol^{-1} (corresponding to a Fe:C-ratio of 5 μmol mol^{-1}, assuming Redfield stoichiometry). Using this ratio, *Johnson et al.* [1997] were able to reproduce a variety of different deep vertical iron profiles with a one-dimensional diffusion-remineralization-scavenging model. It should therefore be close to an average Fe:N-ratio in the remineralization of organic matter, and possibly also to an average uptake ratio. Nevertheless, the Fe:N-ratio in phytoplankton uptake at the BATS site might deviate from such an average, for example, owing to the presence of nitrogen fixers at the BATS site.

[65] We performed a number of model runs, varying the value for the Fe:N-ratio (10, 20, 33, 50, 100, and 200 μmol mol^{-1}) or the Fe:C ratio (2, 5, and 13 μmol mol^{-1}). Surprisingly, the difference between the model runs that assume a constant Fe:C ratio (Figure 9, bottom panel) as compared to the runs assuming a constant Fe:N ratio (Figure 9, top panel) is small, in spite of the fact that the C:N ratio in primary production in the model reaches values more than double the Redfield value in summer. However, this happens during a time where the biological iron uptake is relatively small compared to the iron source from dust deposition.

[66] In summer, therefore, the variation of the Fe:N or Fe:C ratio causes only little change in the concentration of dissolved iron (Figure 9). Only during the spring phytoplankton bloom period, the concentration of dissolved iron decreases with increasing biological uptake. Fe:N-ratios up to 100 μmol mol^{-1} lead to concentrations of dissolved iron that are in the range of observed concentrations. Fe:N-ratios above 150 μmol mol^{-1}, in

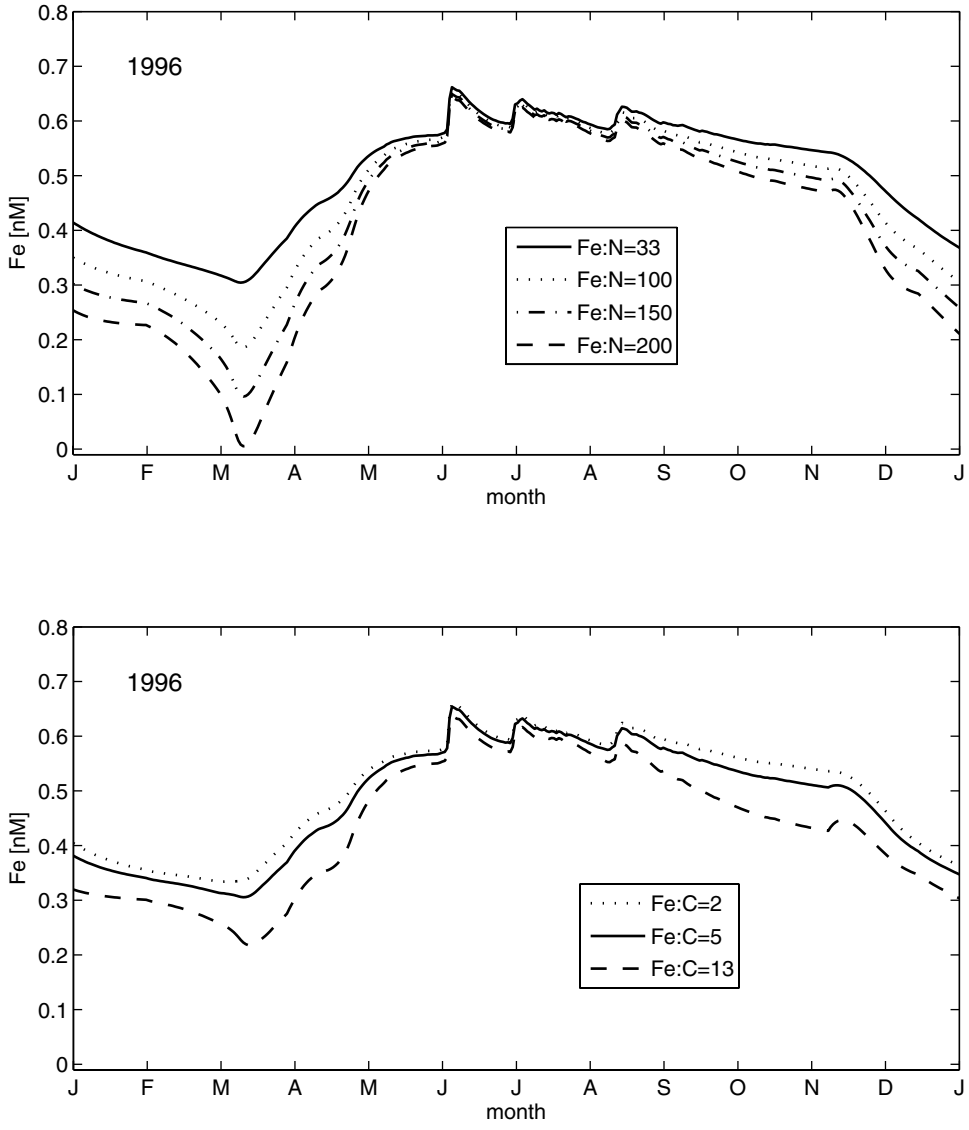

Figure 9. Total Fe concentration (year 1996) of model runs (top) with varying Fe:N-ratio (μmol mol^{-1}) in phytoplankton or (bottom) with varying Fe:C-ratio (μmol mol^{-1}).

contrast, lead to iron concentrations tending to zero during the phytoplankton bloom and accordingly to iron-limited conditions. The subtropical Atlantic is not thought to experience regular iron limitation [*Fung et al.*, 2000], owing to ample supply of iron from dust deposition from the surrounding land masses. We therefore assume that the mean Fe:N-ratio at the BATS site does not exceed a value of 150 μmol mol^{-1}.

[67] The balances of the annually averaged fluxes of our model are strongly affected by the elemental ratio. The more iron is taken up, the more iron is entrained by mixing with deeper water and the less iron is scavenged. A 10 times higher Fe:N ratio, for example, leads on average to 2.6 times higher entrainment fluxes and to 0.8 times lower scavenging fluxes. The exchange with deeper water and the reduced scavenging compensate the higher uptake so that the iron concentration remains relatively stable.

[68] The main compensation is again caused by the mixing with deeper water. Owing to the strong seasonal mixed layer cycle, small changes in iron concentration lead to strong changes in vertical iron fluxes (see section 4.1). A decrease in scavenging with increasing Fe:N-ratio is caused by the lower values of [Fe(III)$'$] during the spring bloom, the time when most of the scavenging takes place because of high particle concentrations.

4.3. The Form of Bioavailable and Atmospheric Iron

[69] It is generally assumed that phytoplankton only assimilates dissolved iron. Dissolved iron concentrations in seawater are low because of the low solubility of Fe(III)$'$ in oxygenated seawater [*Byrne and Kester*, 1976], so that the availability of iron can limit phytoplankton productivity [*Bruland et al.*, 1991]. Furthermore, not all forms of iron in seawater are equally available for uptake by phytoplankton.

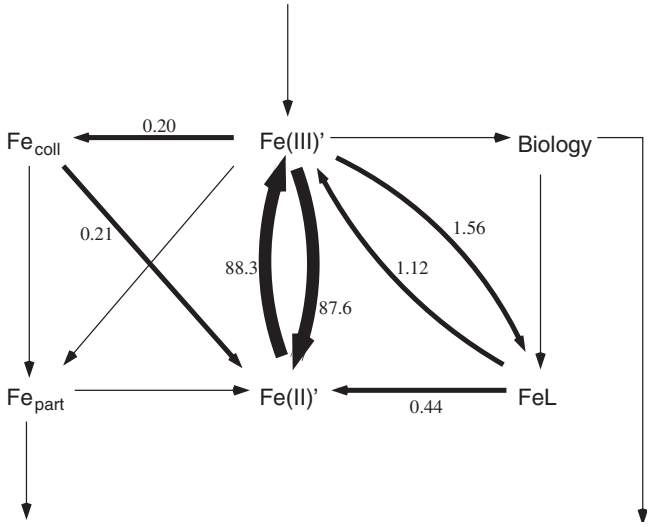

Figure 10. Flux diagram showing the annually averaged rate of change of iron concentrations associated with individual processes (in nM d^{-1}). Arrows without numbers correspond to an average rate of change smaller than 0.01 nM d^{-1}.

Experiments in artificial or UV-digested seawater [*Anderson and Morel*, 1982; *Hudson and Morel*, 1990] have shown a dependency of iron uptake on ferric dissolved inorganic Fe(III)′. However, complexation by strong organic ligands [e.g., *Gledhill and van den Berg*, 1994; *van den Berg*, 1995; *Rue and Bruland*, 1995; *Wu and Luther*, 1995] results in Fe(III)′ concentrations in seawater that are too low to support growth. Uptake of iron bound to organic complexes has been demonstrated [*Soria-Dengg and Horstmann*, 1995; *Maldonado and Price*, 1999, 2001], but cyanobacteria and eucariotes differ in the classes of organic complexes they can access [*Hutchins et al.*, 1999], probably because of different uptake mechanisms. Uptake by eucariotes often involves extracellular iron reductases, a theoretically very efficient iron uptake mechanism [*Völker and Wolf-Gladrow*, 1999]. *Barbeau et al.* [1996] suggested that microbial protozoan grazers can solubilize colloidal iron. Results by *Nodwell and Price* [2001] and *Chen et al.* [2003] show a direct uptake of colloidal iron.

[70] We therefore modified our model by varying the form of iron (Fe(III)′, Fe(II)′, FeL, or Fe_{col}) that is actually taken up by phytoplankton during its growth, to study whether this has an effect on the iron biogeochemistry in the mixed layer. These model changes, however, have hardly any effect on model results. The concentration differences between model runs are maximally 0.01 nM and therefore are far from causing iron limiting conditions. The reason for that negative result is that the biological iron uptake rate reaches maximally 0.01 nM d^{-1} during the bloom, while the photochemical rates of cycling between different iron forms are 1 to 4 order of magnitudes higher (Figure 10). The uptake is a relatively slow process compared to the rapid iron cycling between its different forms, so that the cycling assures enough supply of iron whichever form of iron is taken up.

[71] The model has a similarly weak sensitivity on the form of atmospheric iron. *Zhuang et al.* [1992] suggested that up to 50% of iron in rainwater is dissolved Fe(II) due to low pH-values and photoreduction in atmospheric water. *Zhu et al.* [1997] assumed that only 1–2% is reduced to Fe(II) during the atmospheric transport. *Jickells and Spokes* [2001] concluded that the form of iron that dominates in atmospheric iron depends on the source of dust, the duration of transport, and the intensity of the atmospheric processes. We changed our model in varying the form of the deposited iron ([Fe(III)′], [Fe(II)′], [FeL] or [Fe_{col}]) to investigate whether this has an effect on the iron biogeochemistry in the mixed layer. The model results are only slightly affected by which form of iron is deposited and only in times of high iron input. The concentration difference of total dissolved iron in the mixed layer is maximally 1 pM depending on which form of iron is deposited. The annual mean rate of change of the iron concentration in the mixed layer due to atmospheric deposition varies between 0.0007 and 0.0013 nM per day (maximal rate 0.08 nM d^{-1} during dust deposition events in summer), which is much smaller than the cycling rates (see above) between the iron forms. Hence whatever form of iron is deposited, the fast cycling of iron between its different forms ensures that neither the concentration and speciation of iron nor the iron fluxes are significantly affected.

4.4. Aggregation of Colloids

[72] Colloids are a size class between soluble chemical species and sinking particles [*Wells and Goldberg*, 1992]. In this study, colloidal iron is defined by the filter cutoffs 0.02–0.4 μm used by *Wu et al.* [2001]. The aggregation of marine colloidal matter is an important mechanism for transferring dissolved substances into the macro-particle size range [*Farley and Morel*, 1986; *Honeyman and Santschi*, 1989]. The stability of colloids is mainly influenced by chemical interactions with particulate surfaces [*Stumm*, 1992]. In spite of low particle concentrations in the open ocean, it is suggested that marine colloids are very dynamic with high colloidal aggregation rates [*Moran and Buesseler*, 1992; *Baskaran et al.*, 1992]. Colloid aggregation and scavenging have been suggested by *Wu and Boyle* [2002] to explain part of the gradient in total dissolved iron concentration between Bermuda and Bahamas.

[73] To investigate the role of colloidal aggregation on the transfer of iron to sinking particles, we compared model results which were produced with and without colloidal aggregation. A further uncertainty is that the photoreactivity of iron on marine particles (and therefore of the newly formed aggregates) is to the best of our knowledge not very well constrained. Iron tends to build strong inner-sphere surface complexes with particles [*Stumm*, 1992] that are probably not very photoreactive. We therefore performed both model runs (with and without aggregation) twice, varying the photoreduction rate of iron on particles, k_{ph4}, between that of colloidal iron, k_{ph1},and zero.

[74] Without colloidal aggregation the modeled total iron concentrations do not differ between the runs with and without photoreduction of particle-bound iron (Figure 11).

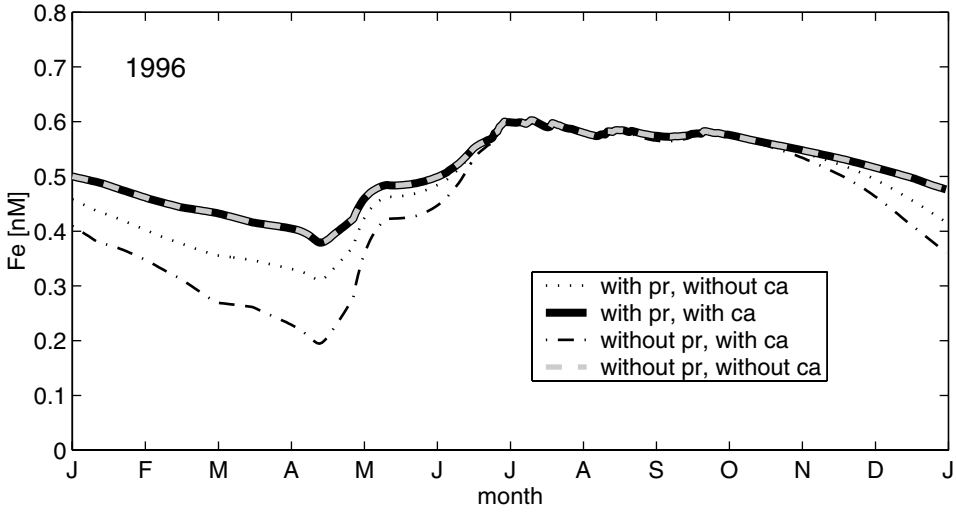

Figure 11. Total Fe concentration (year 1996) of model runs with and without colloidal aggregation (ca) as well as with and without photoreduction of particles (pr).

The particle concentration at the BATS site is so low that without colloid aggregation, the scavenging of iron becomes negligible compared to the fluxes by atmospheric input, biological uptake, and exchange with deeper water.

[75] With colloidal aggregation the iron concentrations during the spring bloom are significantly lower (on average 26% with photochemical reduction of particle-bound iron, and 57% without) than without (see Figure 11). With colloidal aggregation, the average total loss of iron by adsorption of iron onto sinking particles is -72×10^{-3} μmol m^2 d^{-1} with photochemical reduction of particle-bound iron, and 171×10^{-3} μmol m^2 d^{-1} without, about 2 orders of magnitude larger than without aggregation. This increased loss through aggregation is compensated by exchange fluxes from below. The exchange flux increases because of the lowered iron concentration during the spring bloom that leads to a smaller loss of iron during the mixed layer shoaling in late spring.

[76] It is obvious that we need to know more about aggregation rates and the photoreactivity of iron bound to particulate surfaces to determine the role of colloid aggregation in the cycling of iron. Nevertheless, the sensitivity study suggests that the fate of dissolved organic matter exuded by phytoplankton and its role in colloidal aggregation is expected to strongly influence the iron speciation process and thus iron availability for algal growth.

4.5. Influence of Cu on the Concentration of Reactive Oxygen Species and on Fe(II) Levels

[77] The strong daily cycle of iron speciation and the high concentrations of Fe(II)′ reached during the day are mostly a consequence of the photochemical production of superoxide. We inferred the necessary rate of photochemical superoxide production from observed concentrations of hydrogen peroxide. Superoxide itself has a very short lifetime and has not, to our knowledge, been measured at the BATS site. There is, however, a possible flaw in the indirect constraint of superoxide concentration by observations of hydrogen peroxide: The reaction from superoxide to hydrogen peroxide can be catalyzed by several other transition metals besides iron. In seawater this is primarily done by copper via the two coupled reactions [*Voelker and Sedlak*, 1995]

$$O_2^- + \mathrm{Cu(II)} \rightarrow O_2 + \mathrm{Cu(I)} \tag{3}$$

$$O_2^- + \mathrm{Cu(I)} + 2H_2O \rightarrow H_2O_2 + \mathrm{Cu(II)} + 2OH^-. \tag{4}$$

[78] To investigate the influence of copper on the strength of the daily cycle of superoxide concentration and iron speciation, rate expressions corresponding to reaction equations (3) and (4) were added to the evolution equations for hydrogen peroxide (18) and superoxide (17), with reaction rates taken from *Voelker and Sedlak* [1995] (Table 3). The concentrations of Cu(I) and Cu(II) were determined from the total Cu concentration, assuming the two reactions (3) and (4) to be in steady state.

[79] Total copper concentrations at the BATS site are around 1 nM, with somewhat higher concentrations in summer. Most of that copper is bound to strong organic ligands, but in summer, there is a weak excess of copper over ligand concentrations [*Moffett*, 1995]. *Voelker and Sedlak* [1995] have shown that reaction rates of organically complexed Cu(II) with O_2^- are orders of magnitude lower than for free cupric ion Cu^{2+}. We therefore performed two sensitivity experiments Cu1 and Cu2, the first assuming that all copper is complexed by some organic ligands, the other assuming that all Cu(II) is present as the free cupric ion Cu^{2+}. We re-adjusted the photochemical production rate of O_2^- ($S_{O_2^-}$) in these experiments in order to compensate for the increase in [H_2O_2] due to reactions (3) and (4).

[80] The additional catalytic pathway for O_2^- dismutation lowers the maximum mid-day summer [O_2^-] values from 0.7 nM for the reference experiment to 0.1 nM in Cu1 and even 1.5×10^{-4} nM in Cu2 (Figure 12). This decrease in [O_2^-] causes a similar but weaker decrease in maximum

Table 3. Additional or Changed Model Parameters in Experiments Cu1 and Cu2

Parameter	Symbol	Unit	Cu1	Cu2
Total Cu concentration	Cu_T	nM	1	1
Cu(I) oxidation rate by O_2^-	k_{cuox}	$nM^{-1}\ d^{-1}$	8.1×10^5	8.1×10^5
Cu(II) reduction rate by O_2^-	k_{cured}	$nM^{-1}\ d^{-1}$	1.4×10^3	6.9×10^5
$[O_2^-]$ production rate at 30 μE $m^{-3}\ s^{-1}$	$S_{O_2^-}$	$nM\ d^{-1}$	778	173

mid-day summer [Fe(II)′] values from 0.45 nM for the reference experiment to 0.3 nM in Cu1 and 0.013 nM in Cu2. In spite of this drastic reduction in [Fe(II)′], both experiments show a strong diurnal cycling of Fe between its different dissolved forms (Figure 13), albeit somewhat smaller than in the reference experiment.

4.6. Role of Excess Ligands

[81] Most determinations of organic complexation of iron in seawater have shown an excess of truly dissolved organic ligands over total dissolved iron [e.g., *Rue and Bruland*, 1995; *van den Berg*, 1995; *Wu and Luther*, 1995; *Witter and Luther*, 1998], leading to picomolar concentrations of Fe(III)′. In the eastern Atlantic, however, *Wu et al.* [2001] have also shown the opposite to occur. The question therefore is how model results would change under a permanent excess of [L_T] over [Fe_T]. Potentially, a permanent ligand excess might change model results considerably, because [Fe(III)′] determines the rates of scavenging, of colloid formation, and of the reduction of iron by superoxide.

[82] The sensitivity of our model results to a permanent ligand excess is studied here by changing the prescribed vertical profile of [L] such that [L_T] below the mixed layer is always at 2 nM. As expected, this change drastically reduces [Fe(III)′] and changes the daily speciation cycle in summer: While the speciation at night in summer was dominated by [Fe(III)′] and [Fe_{col}] in the standard model run (Figure 4), it is dominated by [FeL] in the sensitivity study (Figure 14), followed by [Fe_{col}]. During the day, [Fe(II)′] increases until somewhat after noon, and decreases afterward. Although the increase in [Fe(II)′] is accompanied by a corresponding decrease in [FeL], it is not mainly caused by direct photoreduction of FeL, but by reduction of Fe(III)′ by O_2^-. Fe(III)′ is then replenished by dissociation of the FeL-complex. The amplitude of the daily [Fe(II)′]-cycle is somewhat smaller (about 25% for the specific day chosen in Figure 14) than in the reference run. One may therefore conclude that a change from an excess of iron over ligands to an excess of ligands over iron affects which species are most involved in the daily speciation cycle (Figure 15). The strength of the cycle itself is hardly altered. The reduced concentration of Fe_{col} and Fe(III)′, compared to the situation with excess iron, decreases the rate at which iron is lost from the mixed layer by the aggregation of colloids and the scavenging of iron onto sinking particles. The total loss of iron via these pathways is 46% lower in the

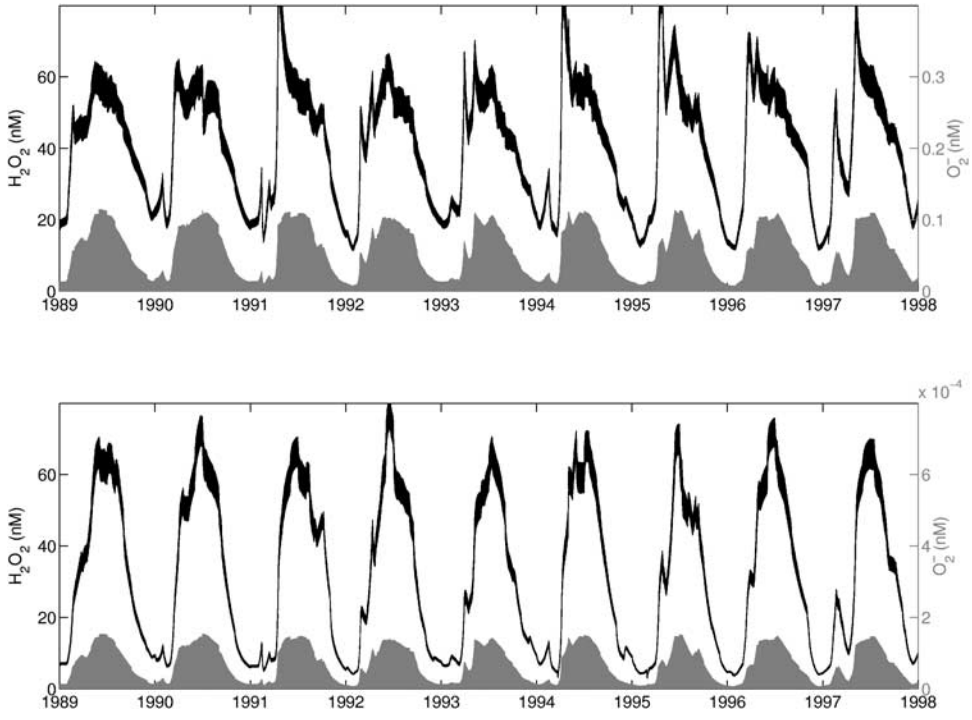

Figure 12. Modeled concentrations of hydrogen peroxide (black), and of superoxide (gray) with catalytic superoxide dismutation by Cu. (top) Experiment Cu1. (bottom) Experiment Cu2. Note the different scale for the two concentrations.

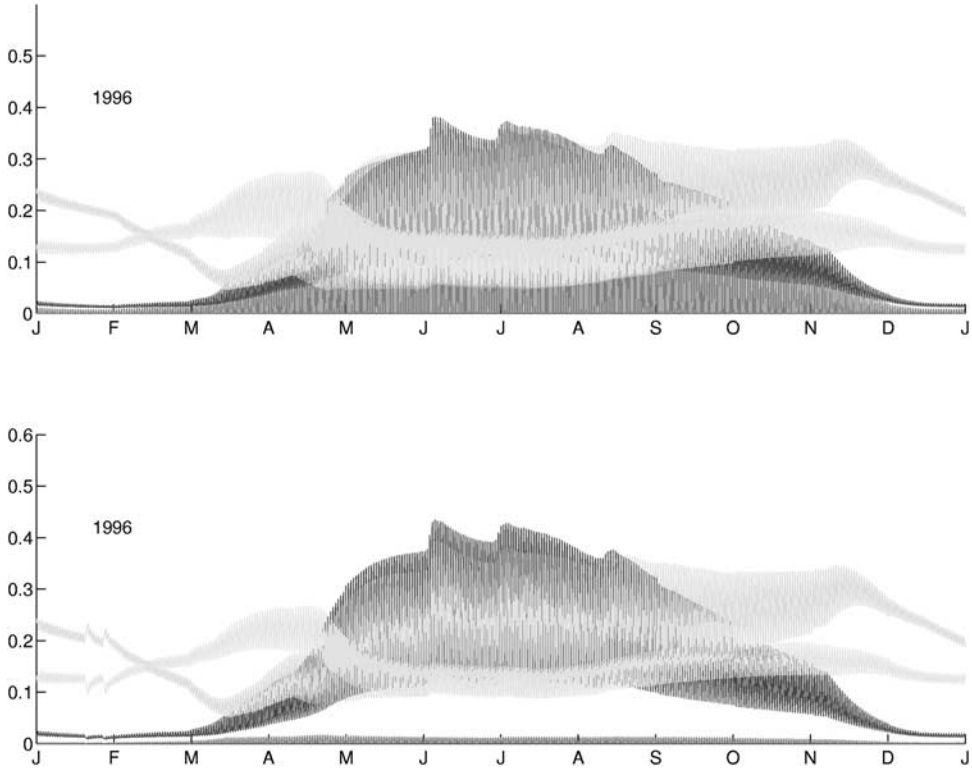

Figure 13. Modeled concentrations of Fe(III)′ (blue), Fe(II)′ (red), Fe_{coll} (green), and FeL (cyan) with catalytic superoxide dismutation by Cu. (top) Experiment Cu1. (bottom) Experiment Cu2. See color version of this figure at back of this issue.

sensitivity run than in the standard model run. However, since the fluxes of iron at the BATS site are dominated by water mass mixing, dust deposition, and net biological consumption, this does not influence the modeled total iron concentration and its annual cycle significantly.

5. Summary and Conclusions

[83] A zero-dimensional model was constructed that describes the cycling of iron between its various physical (dissolved, colloidal, particulate) and chemical (redox state and organic complexation) forms in the oceanic mixed layer. The model is coupled to a simple ecosystem model and is driven by observed or modeled values of dust deposition, mixed layer depth, temperature, and solar irradiation from the Bermuda Atlantic Time-series Study (BATS).

[84] Despite its simplicity, the ecosystem model did reasonably well in reproducing chlorophyll *a* concentrations and primary production data from BATS. This was achieved by applying an optimization algorithm to determine a best parameter set for the ecosystem model and by using a parameterization for variable C:N phytoplankton nutrient utilization rates, which became important as soon as phytoplankton ran into nitrogen limitation. The annual

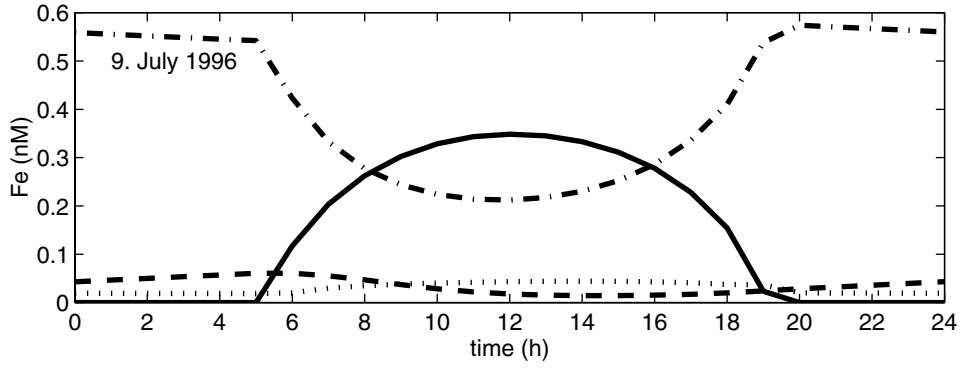

Figure 14. Daily cycle of iron speciation for 9 July 1996 (compare to Figure 4) with permanent excess of organic ligands ($[L_{tot}] \approx 2$ nM) over dissolved iron concentrations.

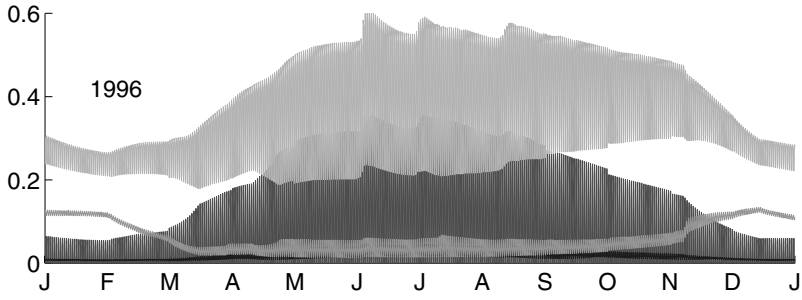

Figure 15. Modeled concentrations of Fe(III)′ (blue), Fe(II)′ (red), Fe_{coll} (green), and FeL (cyan) with permanent excess of organic ligands ($[L_{tot}] \approx 2$ nM) over dissolved iron concentrations. See color version of this figure at back of this issue.

export production is somewhat on the high side of the available data-based estimates. The model underestimates the concentration of particulate organic nitrogen in summer, probably owing to the absence of an explicitly modeled microbial loop.

[85] Model results show total dissolved iron concentrations that are in good agreement with observed values [*Wu and Luther*, 1995; *Wu and Boyle*, 2002]. Modeled annual average fluxes of iron are also within the (still pretty broad) limits of data-based estimates [*Jickells*, 1999], but depend strongly on relatively uncertain parameter values. Our model results, however, show an important role of the vertical flux of iron due to the entrainment and detrainment of water during the annual cycle of mixed layer deepening and shoaling. This flux is dominant in the sense that it balances the other fluxes in such a way that the total dissolved iron concentration in the mixed layer at the BATS site does not depend strongly on the size of, for example, dust input, but remains tightly coupled to the concentration below the mixed layer. This result clearly depends on the strength of the annual mixed layer cycle and cannot be generalized to other more quiet oceanic regions.

[86] The primary aim of this study was to get a better qualitative understanding of the role of iron speciation and the processes influencing it for the biogeochemical cycling of iron. Since there is little data on iron speciation and its temporal evolution at the BATS site, our conclusions here follow from a number of sensitivity studies with the model and are of a more qualitative nature. Nevertheless, we think we can give the following answers to the set of questions listed in the introduction:

[87] 1. How strong is the daily photochemical redox-cycling of iron at the BATS site? How important is the direct photoreduction of iron species compared to the reduction by photoproduced superoxide? Is there an influence of other transition metals on the strength of the redox cycle?

[88] Regardless of details of the chemical model, the daily irradiance cycle drives a strong cycle of iron speciation. This cycle is characterized by concentrations of Fe(II)′ that more or less follow the irradiance cycle (with maximum values attained somewhat later than noon). During the night, the speciation is dominated by various ferric iron species. The increase of [Fe(II)′] during the day is primarily driven by the reduction of Fe(III)′ by photoproduced superoxide, with direct photoreduction of organically complexed Fe(III) or other ferric iron species being much weaker. The maximum value of [Fe(II)′] reached during the day depends strongly on the chemical environment (mainly on the concentration and degree of organic complexation of copper, and on the rate of photochemical production of superoxide, less on the presence of organic ligands for iron), but a strong diurnal cycling of Fe between its different dissolved forms was found in all model experiments. Our model results therefore suggest that daylight concentrations of Fe(II)′ in the surface ocean will depend on local conditions such as presence of copper and colored dissolved organic matter, but that nevertheless the photochemically driven cycling of iron between its various chemical forms is generally quite rapid. The photochemical reactivity of organic complexes of iron seems to be of little importance for this cycling.

[89] 2. Under which conditions can colloid aggregation lead to a significant loss of iron from the surface layer of the ocean?

[90] We have not attempted here a full model of colloid formation and aggregation, but restricted ourselves to modeling the formation of inorganic iron-containing colloids and their aggregation onto larger sinking particles. Bearing that in mind, and that the aggregation rate has been extrapolated from measurements at much higher particle concentrations, the model results suggest that aggregation of colloids is an important process even in the open ocean, which can lead to significant iron removal from the mixed layer. Whether the iron that adsorbs on sinking particles by aggregation of colloids is exported out of the mixed layer, however, also depends on the photochemical lability of the adsorbed iron, which is, to the best of our knowledge, not constrained.

[91] 3. How strong is the influence of the solubility and the chemical form of dust-deposited iron?

[92] In our model results, increasing the percentage of dissolvable iron in dust increases the concentration of iron in the mixed layer mainly in summer, when the mixed layer is shallow. The annual mean concentration of iron is much less sensitive to the solubility. In an annual average the variation of iron input by variation of the solubility of iron in dust is compensated by the iron flux via exchange with

deeper waters, especially during the strong vertical mixing in winter. However, solubilities of atmospheric iron of more than 2.5% lead to summer dissolved iron concentrations that are incompatible with observations. The small sensitivity of the average dissolved iron concentration at the BATS site to the value of the solubility is caused by the very strong vertical exchange associated with the mixed layer cycle at the BATS site and cannot be generalized to more stratified oceanic regimes. There has been some debate over which chemical species of iron is prevalent in dust deposition, especially in wet deposition. In our model results, however, the speciation of deposited iron makes no significant difference to the model results. Whatever form of iron is deposited, the rapid daily cycling of iron between its different forms assures that neither the concentration and speciation of iron nor the iron fluxes are significantly affected.

[93] 4. Does it make a difference to the iron cycle which chemical form of iron is taken up by phytoplankton? How sensitive are model results to changes in the Fe:N or Fe:C-ratio of phytoplankton uptake?

[94] Changes in the Fe:N ratio in organic matter do not affect modeled total dissolved Fe concentrations strongly. They lead to corresponding changes in the vertical biologically mediated flux of iron, but these changes are compensated by the same mechanism as changes in dust iron solubility, namely by exchange with water masses from below the mixed layer. Only for Fe:N ratios above 150 μmol mol^{-1} we obtain iron concentrations during the phytoplankton bloom that would limit phytoplankton growth. This is generally not assumed to happen at the BATS site. The insensitivity of modeled iron concentrations to the Fe:N ratio is again not valid for the ocean generally, but is due to the strong vertical exchange at the BATS site. However, a more general conclusion is that from the point of view of the dissolved iron chemistry, it makes no significant difference whether phytoplankton cells take up Fe(III)′, Fe(II)′, or FeL. The rapid cycling of iron between its different dissolved forms ensures that any pool that is depleted by biological uptake gets replenished quickly. This is mainly an effect of the redox-reactivity of iron with respect to superoxide and on the daily concentration cycle of superoxide. It does not mean, on the other hand, that the preference of phytoplankton for the one or the other form of dissolved iron cannot have biogeochemical consequences: We have assumed here that phytoplankton growth is unlimited by iron availability, but in reality, the uptake rate of any chemical species depends on its concentration in the medium, which would be different for the different iron species. This is likely to be of importance in iron-limited ocean regimes.

[95] Many of the still qualitative statements above could be made more quantitative if we had more data to validate the model predictions. A data set of time-resolved iron speciation data including measurements of Fe(II)′ and H_2O_2, and also some information on the concentration and organic complexation of copper, would be most useful.

[96] We expect that modeling a more stratified oceanic region than at the BATS site would yield modeled iron concentrations that are much more sensitive to parameters such as the solubility of iron in dust or the colloid aggregation rate. Validating such model results therefore has more potential to constrain these parameters.

[97] We realize that further model development is required. This concerns the following.

[98] 1. There exists a simplistic assumption of uniform concentrations within the mixed layer. The short timescale of photochemical processes can lead to vertical concentration differences within the mixed layer that can only be represented with a depth-dependent physical model.

[99] 2. There is a simplistic representation of photochemical reactions with reactions being assumed to vary with irradiance over the visible band. In reality, ultraviolet radiation is probably also important, but much more attenuated with depth.

[100] 3. There is still a very simple representation of the cycling of organic iron ligands. The last two improvements, however, will need further information from laboratory and field experiments with regard to the quantum yield of the different photochemical processes, and to the origin and fate of organic ligands for iron present in seawater.

Appendix A: Model Equations

[101] Three biological model equations determine the evolution of the concentrations of phytoplankton P, detritus D, and dissolved inorganic nitrogen N. They are formulated in units of μM nitrogen d^{-1}.

$$\frac{d}{dt}P = (\mu - \rho_P \eta_T)P - \Phi_P^* P^2 - \frac{m_r + h^+}{H}P, \tag{A1}$$

$$\frac{d}{dt}D = \Phi_P^* P^2 - \gamma_D \eta_T D - \frac{m_r + h^+ + w_s}{H}D, \tag{A2}$$

$$\frac{d}{dt}N = -(\mu - \rho_P \eta_T)P + \gamma_D \eta_T D + \frac{m_r + h^+}{H}\left(N_{deep} - N\right). \tag{A3}$$

The phytoplankton growth rate μ is the smaller of either a nutrient- or a light-limited growth rate $\mu = \min(\mu_N, \mu_L)$. Here $\mu_N = \mu^* \eta_T N/(K_N + N)$ has the standard Michaelis-Menten dependency on nitrogen availability, multiplied by a temperature dependency η_T of the maximum growth rate μ*. For η_T we choose $\eta_T = (C_{ref})^{T[^\circ C]^{-1}}$ as per *Fasham* [1993]. Here $\mu_L = \mu^* \eta_T f(\alpha, I, H, \lambda)$ is the light-limited growth function following *Evans and Parslow* [1985] that depends on the slope of the photosynthesis-irradiance curve α, the daily averaged irradiance at the sea surface I, the mixed layer depth H, and the light attenuation λ. Concentrations within the mixed layer change by mixing at the base of the mixed layer with rate m_r, and by entrainment of water during mixed layer deepening h^+, where

$$h^+ = \max\left(\frac{dH}{dt}, 0\right). \tag{A4}$$

Detrital material is lost out of the mixed layer by sinking, for which we assume a constant sinking speed w_s. N_{deep} is

the nitrogen concentration below the mixed layer, which we parameterize as in work by *Schartau et al.* [2001].

[102] Although the model is formulated in nitrogen units, we allow for a variable chlorophyll:carbon ratio $r_{Chl:C}$ in phytoplankton biomass (in the dimension mg Chl mg C^{-1}) following *Cloern* [1995],

$$r_{Chl:C} = 0.003 + 0.0154 \exp\left(0.05\, T[^\circ C]^{-1}\right) \quad \text{(A5)}$$

$$times \frac{N}{K_N + N} \times \exp\left(\frac{-0.059\, I_{PAR}(1 - \exp(-\lambda H))}{\lambda H}\right), \quad \text{(A6)}$$

where $\lambda = k_w + \kappa Chl$ is the light attenuation by water and chlorophyll, and $I_{PAR} = f_{PAR} I$ is the irradiance within the photosynthetically active range.

[103] We also parameterize the carbon:nitrogen ratio $r_{C:N}$ in phytoplankton primary production by

$$r_{C:N} = Q_{\min} + (Q_{\max} - Q_{\min}) \times \left(1 - \exp\left(\frac{-\sigma(\mu_L - \mu)}{\mu}\right)\right). \quad \text{(A7)}$$

This parameterization ensures that phytoplankton grows at a ratio $Q_{\min}$ under light limitation, while nutrient limitation increases $r_{C:N}$ up to the limit $Q_{\max}$.

[104] The concentration of inorganic particles A in the mixed layer (in mg L^{-1}) is determined from a balance between dust deposition and loss out of the mixed layer by mixing, entrainment, and sinking,

$$\frac{d}{dt}A = \frac{F_{dust}}{H} - \frac{m_r + h^+ + w_s}{H}A, \quad \text{(A8)}$$

where we assume the same sinking speed for inorganic particles as for detritus. F_{dust} is the dust deposition flux per unit area of the sea surface.

[105] The equations for the concentration of the three truly dissolved iron species Fe(III)′, Fe(II)′, and FeL (in units nM iron d^{-1}) are

$$\begin{aligned}\frac{d}{dt}[\mathrm{Fe(III)}'] = {} & \frac{F_{Fe}}{H} + k_{ld}[\mathrm{FeL}] + (k_{ox1}[\mathrm{O_2}] \\ & + k_{ox2}[\mathrm{O_2^-}] + k_{ox3}[\mathrm{H_2O_2}])[\mathrm{Fe(II)}'] \\ & - (k_{col} + k_{ph3} + k_{fel}[\mathrm{L}] + k_{red}[\mathrm{O_2^-}] \\ & + k_{sca}(r_{m:N}D + A))[\mathrm{Fe(III)}'] - \frac{m_r + h^+}{H}[\mathrm{Fe(III)}'],\end{aligned} \quad \text{(A9)}$$

$$\begin{aligned}\frac{d}{dt}[\mathrm{Fe(II)}'] = {} & + (k_{red}[\mathrm{O_2^-}] + k_{ph3})[\mathrm{Fe(III)}'] - \mu PR_{Fe:N} + k_{ph1}[\mathrm{Fe_p}] \\ & + k_{ph1}[\mathrm{Fe_{col}}] + k_{ph2}[\mathrm{FeL}] - (k_{ox1}[\mathrm{O_2}] + k_{ox2}[\mathrm{O_2^-}] \\ & + k_{ox3}[\mathrm{H_2O_2}])[\mathrm{Fe(II)}'] - \frac{m_r + h^+}{H}[\mathrm{Fe(II)}'],\end{aligned} \quad \text{(A10)}$$

$$\begin{aligned}\frac{d}{dt}[\mathrm{FeL}] = {} & k_{fel}[\mathrm{Fe(III)}'][\mathrm{L}] + r_{Fe:N}(\gamma_D D + \rho_P P) \\ & - (k_{ld} + k_{ph2})[\mathrm{FeL}] + \frac{m_r + h^+}{H}\left([\mathrm{FeL}]_{deep} - [\mathrm{FeL}]\right).\end{aligned} \quad \text{(A11)}$$

Equations (A7) and (A8) are coupled by the oxidation of Fe(II)′ by O_2, O_2^- and H_2O_2, and by the reduction of Fe(III)′ by O_2^- and by light. Equations (A7) and (A9) are coupled by the formation and dissociation of the organic complex, and equations (A8) and (A9) are coupled by the photodissociation of the organic complex. F_{Fe} is the flux of dissolved iron per unit area by to dust deposition at the sea surface. Here we assume that dust input is a source of Fe(III)′, but we have also performed model experiments where dust is a source of Fe(II)′, FeL, or Fe_{col}. The biological uptake of iron is $-\mu PR_{Fe:N}$, where the Fe:N-ratio is either the constant $r_{Fe:N}$ or calculated as $R_{Fe:N} = r_{Fe:C} r_{C:N}$, while the flux of iron due to remineralization of organic matter is $r_{Fe:N}(\gamma_D D + \rho_P P)$. All photochemical rates k_{phN}, $N = 1, 4$ are assumed to be proportional to the instantaneous irradiance, averaged over the mixed layer depth.

[106] Equations (A7) to (A9) are complemented by equations for colloidal iron and iron adsorbed onto sinking particles,

$$\begin{aligned}\frac{d}{dt}[\mathrm{Fe_{col}}] = {} & k_{col}[\mathrm{Fe(III)}'] - (k_{ph1} + k_{ag}(r_{m:N}D + A)) \times [\mathrm{Fe_{col}}] \\ & + \frac{m_r + h^+}{H}\left([\mathrm{Fe_{col}}]_{deep} - [\mathrm{Fe_{col}}]\right)\end{aligned} \quad \text{(A12)}$$

$$\begin{aligned}\frac{d}{dt}[\mathrm{Fe_p}] = {} & (r_{m:N}D + A)(k_{sca}[\mathrm{Fe(III)}'] + k_{ag}[\mathrm{Fe_{col}}]) \\ & - k_{ph4}[\mathrm{Fe_p}] - \frac{m_r + h^+ + w_s}{H}[\mathrm{Fe_p}].\end{aligned} \quad \text{(A13)}$$

As did *Johnson et al.* [1994], we model the formation of colloidal iron in (14) as a first-order process in [Fe(III)′]. Colloidal iron is solubilized by photoreduction and aggregates to larger sinking particles. We assume that the dominant aggregation process is due to collisions with larger particles and model it as a first-order process both in $[Fe_{col}]$ and the total particle concentration $r_{m:N} D + A$, where $r_{m:N}$ is a conversion factor from concentrations in M nitrogen to g L^{-1}. The scavenging of Fe(III)′ onto sinking particles is modeled similarly as first-order in [Fe(III)′] and in $r_{m:N}D + A$.

[107] There is still debate over both the sources and the fate of strong organic iron-binding ligands in the ocean. The similarity in binding strength of ligands and of some phytoplankton compounds [*Witter et al.*, 2000] suggests that they may be released during cell lysis and grazing [*Hutchins et al.*, 1995]. However, lab experiments also show that cyanobacteria release ligands, so-called siderophores, into the medium to make iron available to them [*Wilhelm and Trick*, 1994; *Wilhelm et al.*, 1996, 1998]. At least part of ligands are broken down photochemically [*Barbeau et al.*, 2001, 2003], but it is unknown to what extent consumption by bacteria is an important loss.

[108] Given these uncertainties, we have decided to model the time evolution of ligands with a simplified equation that lacks a biological source of free ligands, but also lacks photochemical degradation, i.e., assumes that photoreduction of FeL produces free ligands.

$$\begin{aligned}\frac{d}{dt}[\mathrm{L}] = {} & (k_{ld} + k_{ph2})[\mathrm{FeL}] - k_{fel}[\mathrm{Fe(III)}'][\mathrm{L}] \\ & + \frac{m_r + h^+}{H}\left([\mathrm{L}]_{deep} - [\mathrm{L}]\right).\end{aligned} \quad \text{(A14)}$$

This ad-hoc parameterization prevents unrealistically low concentrations of [FeL] + [L] in the mixed layer to occur owing to photochemical degradation.

[109] The system of equations is completed by specifying the concentrations of oxygen, superoxide, and hydrogen peroxide. At the BATS site, $[O_2]$ varies by about ±7% over the annual cycle. We set $[O_2]$ to a constant value for simplicity. The other two oxidants, however, are strongly influenced by reactions within the iron system and the daily cycle of irradiance. We describe their evolution similarly to *Voelker and Sedlak* [1995] and *Miller et al.* [1995],

$$\frac{d}{dt}\left[O_2^-\right] = S_{O_2^-} + k_{ox1}[O_2]\left[Fe(II)'\right] - 2k_{dm}\left[O_2^-\right]^2 - \left(k_{ox2}\left[Fe(II)'\right] + k_{red}\left[Fe(III)'\right]\right)\left[O_2^-\right] - \frac{m_r + h^+}{H}\left[O_2^-\right] \tag{A15}$$

$$\frac{d}{dt}[H_2O_2] = \frac{F_{H_2O_2}}{H} + k_{dm}\left[O_2^-\right]^2 + k_{ox2}\left[O_2^-\right]\left[Fe(II)'\right] - k_{ox3}[H_2O_2]\left[Fe(II)'\right] - k_{dis}[H_2O_2] - \frac{m_r + h^+}{H}[H_2O_2]. \tag{A16}$$

In (17), the rate of production of superoxide by photoreactions with colored dissolved organic matter $S_{O_2^-}$ is assumed to be proportional to irradiance. For the deposition of H_2O_2 with rain $F_{H_2O_2}$ in (18), we assume a constant concentration of H_2O_2 in rainwater, such that $F_{H_2O_2} = [H_2O_2]_{rain}\ Pr$.

[110] Deep concentrations of the iron species FeL and Fe_{col}, and of free ligands L, are prescribed as linear functions of H using a fit to observed concentration profiles by *Wu et al.* [2001]. All the other species are assumed to have vanishing concentration below the mixed layer.

[111] **Acknowledgments.** Lisa Weber and Christoph Völker received funding for this work from the EU project IRONAGES (contract EVK2-CT1999-00031). We thank Andreas Oschlies and the reviewers for their helpful comments. Lisa also thanks Andreas Oschlies for support.

References

Anderson, M., and F. Morel (1982), The influence of aqueous iron chemistry on the uptake of iron by the coastal diatom *Thalassiosira weissflogii*, *Limnol. Oceanogr.*, *27*, 789–831.

Archer, D., and K. Johnson (1999), A model of the iron cycle in the ocean, *Global Biogeochem. Cycles*, *13*, 269–279.

Arimoto, R. (2001), Eolian dust and climate: Relationships to sources, tropospheric chemistry, transport, and deposition, *Earth Sci. Rev.*, *54*, 29–42.

Armstrong, R. (1999), An optimization-based model of iron-light-ammonium colimitation of nitrate uptake and phytoplankton growth, *Limnol. Oceanogr.*, *44*, 1436–1446.

Aumont, O., E. Maier-Reimer, S. Blain, and P. Monfray (2003), An ecosystem model of the global ocean including Fe, Si, P colimitations, *Global Biogeochem. Cycles*, *17*(2), 1060, doi:10.1029/2001GB001745.

Balistieri, L., P. Brewer, and J. Murray (1981), Scavenging residence times of trace metals and surface chemistry of sinking particles in the deep ocean, *Deep Sea Res., Part A*, *28*, 101–121.

Barbeau, K., and J. Moffett (2000), Laboratory and field studies of colloidal iron oxide dissolution as mediated by phagotrophy and photolysis, *Limnol. Oceanogr.*, *45*, 827–835.

Barbeau, K., J. Moffett, D. Caron, P. Croot, and D. Erdner (1996), Role of protozoan grazing in relieving iron limitation of phytoplankton, *Nature*, *380*, 61–64.

Barbeau, K., E. Rue, K. Bruland, and A. Butler (2001), Photochemical cycling of iron in the surface ocean mediated by microbial iron (III)-binding ligands, *Nature*, *413*, 409–413.

Barbeau, K., E. Rue, C. Trick, K. Bruland, and A. Butler (2003), Photochemical reactivity of siderophores produced by marine heterotrophic bacteria and cyanobacteria based on characteristic Fe(III) binding groups, *Limnol. Oceanogr.*, *48*, 1069–1078.

Baskaran, M., P. Santschi, G. Benoit, and B. Honeyman (1992), Scavenging of thorium isotopes by colloids in seawater of the Gulf of Mexico, *Geochim. Cosmochim. Acta*, *56*(9), 3375–3388.

Bissett, W. P., J. J. Walsh, D. A. Dieterle, and K. L. Carder (1999), Carbon cycling in the upper waters of the Sargasso Sea: I. Numerical simulation of differential carbon and nitrogen fluxes, *Deep Sea Res., Part I*, *46*, 205–269.

Bowie, A., M. Maldonado, R. Frew, P. Croot, E. Achterberg, R. Mantoura, P. Worsfold, C. Law, and P. Boyd (2001), The fate of added iron during a mesoscale fertilisation experiment in the Southern Ocean, *Deep Sea Res., Part II*, *48*, 2703–2743.

Boyd, P., and C. Law (2001), The Southern Ocean Iron Release Experiment (SOIREE)—Introduction and summary, *Deep Sea Res., Part II*, *48*, 2425–2438.

Brock, T. D. (1981), Calculating solar radiation for ecological studies, *Ecol. Modell.*, *14*, 1–19.

Bruland, K., J. Donat, and D. Hutchins (1991), Interactive influences of bioactive trace metals on biological production in natural waters, *Limnol. Oceanogr.*, *36*, 1555–1577.

Byrne, R., and D. Kester (1976), Solubility of hydrous ferric oxide and iron speciation in seawater, *Mar. Chem.*, *4*, 255–274.

Carlson, C., H. W. Ducklow, and A. F. Michaels (1994), Annual flux of dissolved organic-carbon from the euphotic zone in the northwestern Sargasso Sea, *Nature*, *371*, 405–408.

Carroll, D. (1996), Chemical laser modeling with genetic algorithms, *AIAA J.*, *34*, 338–346.

Chen, M., R. Dei, W.-X. Wang, and L. Guo (2003), Marine diatom uptake of iron bound with natural colloids of different orgins, *Mar. Chem.*, *81*, 177–189.

Christian, J., M. Verschell, R. Murtigudde, A. Busalacchi, and C. McClain (2002), Biogeochemical modelling of the tropical Pacific Ocean: II. Iron biogeochemistry, *Deep Sea Res., Part II*, *49*, 509–543.

Cloern, J. (1995), An empirical model of the phytoplankton chlorophyll:-carbon ratio—The conversion factor between productivity and growth rate, *Limnol. Oceanogr.*, *40*, 1313–1321.

Coale, K., et al. (1996), A massive phytoplankton bloom induced by an ecosystem-scale iron fertilization experiment in the equatorial Pacific Ocean, *Nature*, *383*, 495–501.

Cooper, W., R. Zika, R. Petasne, and J. Plane (1988), Photochemical formation of H_2O_2 in natural waters exposed to sunlight, *Environ. Sci. Technol.*, *22*, 1156–1160.

Croot, P., A. Bowie, R. Frew, M. Maldonado, J. Hall, K. Safi, J. L. Roche, P. Boyd, and C. Law (2001), Retention of dissolved iron and Fe^{II} in an iron-induced Southern Ocean phytoplankton bloom, *Geophys. Res. Lett.*, *28*, 3425–3428.

Doney, S. (1996), A synoptic atmospheric surface forcing data set and physical upper ocean model for the U.S. JGOFS Bermuda Atlantic Time-Series Study site, *J. Geophys. Res.*, *101*, 25,615–25,634.

Doney, S., R. Najjar, and S. Stewart (1995), Photochemistry, mixing and diurnal cycles in the upper ocean, *J. Mar. Res.*, *53*, 341–369.

Duce, R., and N. Tindale (1991), Atmospheric transport of iron and its deposition in the ocean, *Limnol. Oceanogr.*, *36*, 1715–1726.

Emmenegger, L., R. Schönberger, L. Sigg, and B. Sulzberger (2001), Light-induced redox cycling of iron in circumneutral lakes, *Limnol. Oceanogr.*, *46*, 49–61.

Evans, G., and J. Parslow (1985), A model of annual plankton cycles, *Biol. Oceanogr.*, *3*, 327–347.

Farley, K., and F. Morel (1986), Role of coagulation in the kinetics of sedimentation, *Environ. Sci. Technol.*, *20*, 187–195.

Fasham, M. (1993), Modelling the marine biota, in *The Global Carbon Cycle*, edited by M. Heimann, pp. 457–504, Springer, New York.

Fennel, K., M. Losch, J. Schroeter, and M. Wenzel (2001), Testing a marine ecosystem model: Sensitivity analysis and parameter optimization, *J. Mar. Syst.*, *28*, 45–63.

Fung, I., S. Meyn, I. Tegen, S. Doney, J. John, and J. Bishop (2000), Iron supply and demand in the upper ocean, *Global Biogeochem. Cycles*, *14*, 281–301.

Geider, R., and J. La Roche (1994), The role of iron in phytoplankton photosynthesis and the potential for iron-limitation of primary productivity in the sea, *Photosynth. Res.*, *39*, 275–301.

Geider, R., H. MacIntyre, and T. Kana (1998), A dynamic regulatory model of phytoplankton acclimation to light, nutrients and temperature, *Limnol. Oceanogr.*, *43*, 679–694.

Gledhill, M., and C. van den Berg (1994), Determination of complexation of iron(III) with natural organic complexing ligands in seawater using cathodic stripping voltammetry, *Mar. Chem.*, *47*, 41–54.

Honeyman, B., and P. Santschi (1989), A Brownian-pumping model for trace metal scavenging: Evidence from Th isotopes, *J. Mar. Res.*, *47*, 951–992.

Hudson, R., and F. Morel (1990), Iron transport in marine phytoplankton: Kinetics of cellular and medium coordination reactions, *Limnol. Oceanogr.*, *35*, 1002–1020.

Hurtt, G. C., and R. A. Armstrong (1996), A pelagic ecosystem model calibrated with BATS data, *Deep Sea Res., Part II*, *43*, 653–683.

Hutchins, D., W.-X. Wang, and N. Fisher (1995), Copepod grazing and the biogeochemical fate of diatom iron, *Limnol. Oceanogr.*, *40*, 989–994.

Hutchins, D., A. Witter, A. Butler, and G. Luther III (1999), Competition among marine phytoplankton for different chelated iron species, *Nature*, *400*, 858–861.

Jickells, T. (1995), Atmospheric input of metals and nutrients to the oceans: Their magnitude and effects, *Mar. Chem.*, *48*, 199–214.

Jickells, T. (1999), The input of dust-derived elements to the Sargasso Sea: A synthesis, *Mar. Chem.*, *68*, 5–14.

Jickells, T., and L. Spokes (2001), Atmospheric iron inputs to the oceans, in *The Biogeochemistry of Iron in Seawater*, edited by D. Turner and K. Hunter, pp. 85–121, John Wiley, Hoboken, N. J.

Jickells, T., W. Deuser, and R. Belastock (1990), Temporal variations in the concentrations of some particulate elements in the surface waters of the sargasso sea and their relationship to deep-sea fluxes, *Mar. Chem.*, *29*, 203–219.

Johnson, K., K. Coale, V. Elrod, and N. Tindale (1994), Iron photochemistry in seawater from the equatorial Pacific, *Mar. Chem.*, *46*, 319–334.

Johnson, K., R. Gordon, and K. Coale (1997), What controls dissolved iron concentrations in the world ocean?, *Mar. Chem.*, *57*, 137–161.

Kieber, R., W. Cooper, J. Wiley, and G. B. Avery Jr. (2001), Hydrogen peroxide at the Bermauda Atlantic Timeseries Station: 1. Temporal variability of atmospheric hydrogen peroxide and its influence on seawater concentrations, *J. Atmos. Chem.*, *39*, 1–13.

Kim, G., and T. Church (2001), Seasonal biogeochemical fluxes of ^{234}Th, and ^{210}Po in the upper Sargasso Sea: Influence from atmospheric iron deposition, *Global Biogeochem. Cycles*, *15*, 651–661.

Kim, G., L. Alleman, and T. Church (1999), Atmospheric depositional fluxes of trace elements, ^{210}Pb, and ^{7}Be to the Sargasso Sea, *Global Biogeochem. Cycles*, *13*, 1183–1192.

King, D., H. Lounsbury, and F. Millero (1995), Rates and mechanism of Fe(II) oxidation at nanomolar total iron concentrations, *Environ. Sci. Technol.*, *29*, 818–824.

Kuma, K., S. Nakabayashi, Y. Suzuki, I. Kudo, and K. Matsunaga (1992), Photo-reduction of Fe(III) by dissolved organic substances and existence of Fe(II) in seawater during spring blooms, *Mar. Chem.*, *37*, 15–27.

Lancelot, C., E. Hannon, S. Becquevort, C. Veth, and H. De Baar (2000), Modeling phytoplankton blooms and carbon export production in the Southern Ocean: Dominant controls by light and iron in the Atlantic sector in Austral spring 1992, *Deep Sea Res., Part I*, *47*, 1621–1662.

Lefevre, N., and A. Watson (1999), Modelling the geochemical cycle of iron in the oceans and its impact on atmospheric CO_2 concentrations, *Global Biogeochem. Cycles*, *13*, 727–736.

Mahowald, N., K. Kohfeld, M. Hansson, Y. Balkanski, S. Harrison, I. Prentice, M. Schulz, and H. Rodhe (1999), Dust sources and deposition during the Last Glacial Maximum and current climate: A comparison of model results with paleodata from ice cores and marine sediments, *J. Geophys. Res.*, *104*, 15,895–15,916.

Maldonado, M., and N. Price (1999), Utilization of iron bound to strong organic ligands by plankton communities in the subarctic North Pacific, *Deep Sea Res., Part II*, *46*, 2447–2473.

Maldonado, M., and N. Price (2001), Reduction and transport of organically bound iron by *Thalassiosira oceanica* (Bacillariophyceae), *J. Phycol.*, *37*, 298–309.

Martin, J. (1990), Glacial-interglacial CO_2 change: The iron hypothesis, *Paleoceanography*, *5*, 1–13.

Martin, J., and S. Fitzwater (1988), Iron deficiency limits phytoplankton growth in the northeast Pacific subarctic, *Nature*, *331*, 341–343.

Martin, J., et al. (1994), Testing the iron hypothesis in ecosystems of the equatorial Pacific Ocean, *Nature*, *371*, 123–129.

Michaels, A., and A. Knap (1996), Overview of the U.S. JGOFS Bermuda Atlantic Timeseries Study and Hydrostation S program, *Deep Sea Res., Part II*, *43*, 157–198.

Miller, W., D. King, J. Lin, and D. Kester (1995), Photochemical redox cycling of iron in coastal seawater, *Mar. Chem.*, *50*, 63–77.

Millero, F., and S. Sotolongo (1989), The oxidation of Fe(II) with H_2O_2 in seawater, *Geochim. Cosmochim. Acta*, *53*, 1867–1873.

Millero, F., S. Sotolongo, and M. Izaguirre (1987), The oxidation kinetics of Fe(II) in seawater, *Geochim. Cosmochim. Acta*, *51*, 793–801.

Moffett, J. (1995), Temporal and spatial variability of copper complexation by strong chelators in the Sargasso Sea, *Deep Sea Res., Part I*, *42*, 1273–1295.

Mongin, M., D. M. Nelson, P. Pondaven, M. A. Brzezinski, and P. Tréguer (2003), Simulation of upper-ocean biogeochemistry with a flexible-composition phytoplankton model: C, N and Si cycling in the western Sargasso Sea, *Deep Sea Res., Part I*, *50*, 1445–1480.

Moore, J., S. Doney, D. Glover, and I. Fung (2001), Iron cycling and nutrient-limitation patterns in surface waters of the world ocean, *Deep Sea Res., Part II*, *49*, 463–507.

Moran, S. B., and K. O. Buesseler (1992), Short residence time of colloids in the upper ocean off Bermuda, *Nature*, *359*, 221–223.

Muggli, D., M. Lecourt, and P. Harrison (1996), Effects of iron and nitrogen source on the sinking rate, physiology and elemental composition of an oceanic diatom from the subarctic Pacific, *Mar. Ecol. Prog. Ser.*, *132*, 215–227.

Nodwell, L., and N. Price (2001), Direct use of inorganic colloidal iron by marine mixotrophic phytoplankton, *Limnol. Oceanogr.*, *46*, 765–777.

Nyffeler, U., Y.-H. Li, and P. Santschi (1984), A kinetic approach to describe trace-element distribution between particles and solution in natural aquatic systems, *Geochim. Cosmochim. Acta*, *48*, 1513–1522.

Obernosterer, I., P. Ruardij, and G. Herndl (2001), Spatial and diurnal dynamics of dissolved organic matter (DOM) fluorescence and H_2O_2 and the photochemical demand of surface water DOM across the subtropical Atlantic Ocean, *Limnol. Oceanogr.*, *46*, 632–643.

O'Sullivan, D., A. Hanson, W. Miller, and D. Kester (1991), Measurement of Fe(II) in surface water of the equatorial Pacific, *Limnol. Oceanogr.*, *36*, 1727–1741.

Parekh, P., M. Follows, and E. Boyle (2004), Modeling the global ocean iron cycle, *Global Biogeochem. Cycles*, *18*, GB1002, doi:10.1029/2003GB002061.

Rose, A., and T. Waite (2003a), Predicting iron speciation in coastal waters from the kinetics of sunlight-mediated iron redox cycling, *Aquat. Sci.*, *65*, 375–383.

Rose, A., and T. Waite (2003b), Kinetics of hydrolysis and precipitation of ferric iron in seawater, *Environ. Sci. Technol.*, *37*, 3897–3903.

Rose, A., and T. Waite (2003c), Kinetics of iron complexation by dissolved natural organic matter in coastal waters, *Mar. Chem.*, *84*, 85–103.

Rue, E., and K. Bruland (1995), Complexation of iron(III) by natural organic ligands in the Central North Pacific as determined by a new competitive ligand equilibration/adsorptive cathodic stripping voltammetric method, *Mar. Chem.*, *50*, 117–138.

Schartau, M., and A. Oschlies (2003a), Simultaneous data-based optimization of a 1D-ecosystem model at three locations in the North Atlantic Ocean: I. Method and parameter estimates, *J. Mar. Res.*, *61*, 765–793.

Schartau, M., and A. Oschlies (2003b), Simultaneous data-based optimization of a 1D-ecosystem model at three locations in the North Atlantic Ocean: II. Standing stocks and nitrogen fluxes, *J. Mar. Res.*, *61*, 795–821.

Schartau, M., A. Oschlies, and J. Willebrand (2001), Parameter estimates of a zero-dimensional ecosystem model applying the adjoint method, *Deep Sea Res., Part II*, *48*, 1769–1800.

Soria-Dengg, S., and U. Horstmann (1995), Ferrioxamines B and E as iron sources for the marine diatom *Phaeodactylum tricornutum*, *Mar. Ecol. Prog. Ser.*, *127*, 269–277.

Spitz, Y. H., J. R. Moisan, and M. R. Abbott (2001), Configuring an ecosystem model using data from the Bermuda Atlantic Time Series (BATS), *Deep Sea Res., Part II*, *48*, 1733–1768.

Spokes, L., and T. Jickells (1996), Factors controlling the solubility of aerosol trace metals in the atmosphere and on mixing into seawater, *Aquat. Geochem.*, *1*, 355–374.

Stumm, W. (1992), *Chemistry of the Solid-Water Interface*, Wiley-Interscience, Hoboken, N. J.

Sunda, W., and S. Huntsman (1995), Iron uptake and growth limitation in oceanic and coastal phytoplankton, *Mar. Chem.*, *50*, 189–206.

Sunda, W., and S. Huntsman (1997), Interrelated influence of iron, light and cell size on marine phytoplankton growth, *Nature*, *390*, 389–392.

van den Berg, C. (1995), Evidence for organic complexation of iron in seawater, *Mar. Chem.*, *50*, 139–157.

Voelker, B., and D. Sedlak (1995), Iron reduction by photoproduced superoxide in seawater, *Mar. Chem.*, *50*, 93–102.

Völker, C., and D. Wolf-Gladrow (1999), Physical limits on iron uptake mediated by siderophores or surface reductases, *Mar. Chem.*, *65*, 227–244.

Waite, T., R. Szymczak, Q. Espey, and M. Furnas (1995), Diel variations in iron speciation in northern Australian shelf waters, *Mar. Chem.*, *50*, 79–91.

Watson, A. (2003), Iron limitation in the ocean, in *The Biogeochemistry of Iron in Seawater*, edited by D. R. Turner and K. A. Hunter, pp. 9–39, John Wiley, Hoboken, N. J.

Wells, M. (2003), The level of iron enrichment required to initiate diatom blooms in HNLC waters, *Mar. Chem.*, *82*, 101–114.

Wells, M., and E. Goldberg (1992), Marine submicron particles, *Mar. Chem.*, *40*, 5–18.

Wells, M., and E. Goldberg (1993), Colloid aggregation in seawater, *Mar. Chem.*, *41*, 353–358.

Wells, M., and L. Mayer (1991), The photoconversion of colloidal iron oxyhydroxides in seawater, *Deep Sea Res.*, *38*, 1379–1395.

Wen, L.-S., P. Santschi, and D. Tang (1997), Interactions between radioactively labeled colloids and natural particles: Evidence for colloidal pumping, *Geochim. Cosmochim. Acta*, *61*, 2867–2878.

Wilhelm, S., and C. Trick (1994), Iron-limited growth of cyanobacteria: Multiple siderophore production is a common response, *Limnol. Oceanogr.*, *39*, 1979–1984.

Wilhelm, S., D. Maxwell, and C. Trick (1996), Growth, iron requirements, and siderophore production in iron-limited *Synechococcus* PCC 7002, *Limnol. Oceanogr.*, *41*, 89–97.

Wilhelm, S., K. MacAuley, and C. Trick (1998), Evidence for the importance of catechol-type siderophores in the iron-limited growth of a cyanobacterium, *Limnol. Oceanogr.*, *43*, 992–997.

Witter, A., and G. Luther III (1998), Variation in Fe-organic complexation with depth in the northwestern Atlantic Ocean as determined using a kinetic approach, *Mar. Chem.*, *62*, 241–258.

Witter, A., D. Hutchins, A. Butler, and G. Luther III (2000), Determination of conditional stability constants and kinetic constants for strong model Fe-binding ligands in seawater, *Mar. Chem.*, *69*, 1–17.

Wu, J., and E. Boyle (1998), Determination of iron in seawater by high-resolution isotope dilution inductively coupled plasma mass spectrometry after $Mg(OH)_2$ coprecipitation, *Anal. Chim. Acta*, *367*, 183–191.

Wu, J., and E. Boyle (2002), Iron in the Sargasso Sea: Implications for the processes controlling dissolved Fe distribution in the ocean, *Global Biogeochem. Cycles*, *16*(4), 1086, doi:10.1029/2001GB001453.

Wu, J., and G. Luther III (1994), Size-fractionated iron concentrations in the water column of the western North Atlantic Ocean, *Limnol. Oceanogr.*, *39*, 1119–1129.

Wu, J., and G. Luther III (1995), Complexation of Fe(III) by natural organic ligands in the Northwest Atlantic Ocean by a competitive ligand equilibration method and a kinetic approach, *Mar. Chem.*, *50*, 159–177.

Wu, J., E. Boyle, W. Sunda, and L.-S. Wen (2001), Soluble and colloidal iron in the oligotrophic North Atlantic and North Pacific, *Science*, *293*, 847–849.

Yuan, J., and A. Shiller (2001), The distribution of hydrogen peroxide in the southern and central Atlantic Ocean, *Deep Sea Res., Part II*, *48*, 2947–2970.

Zhu, X., J. Prospero, and F. Millero (1997), Diel variability of soluble Fe(II) and soluble total Fe in North African dust in the trade winds at Barbados, *J. Geophys. Res.*, *102*, 21,297–21,305.

Zhuang, G., R. Duce, and D. Kester (1990), The dissolution of atmospheric iron in the surface seawater of the open ocean, *J. Geophys. Res.*, *95*, 16,207–16,216.

Zhuang, G., Z. Yi, R. Duce, and P. Brown (1992), Chemistry of iron in marine aerosols, *Global Biogeochem. Cycles*, *6*, 161–173.

M. Schartau, Marine Sciences Research Center (MSRC), State University of New York at Stony Brook, Stony Brook, NY 11794, USA. (mschartau@notes.cc.sunysb.edu)

C. Völker and D. A. Wolf-Gladrow, Alfred-Wegener-Institut für Polar- und Meeresforschung, Am Handelshafen 12, 27515 Bremerhaven, Germany. (cvoelker@awi-bremerhaven.de; dwolf@awi-bremerhaven.de)

L. Weber, Southampton Oceanography Centre, European Way, Southampton SO14 3ZH, UK. (llw@soc.soton.ac.uk)

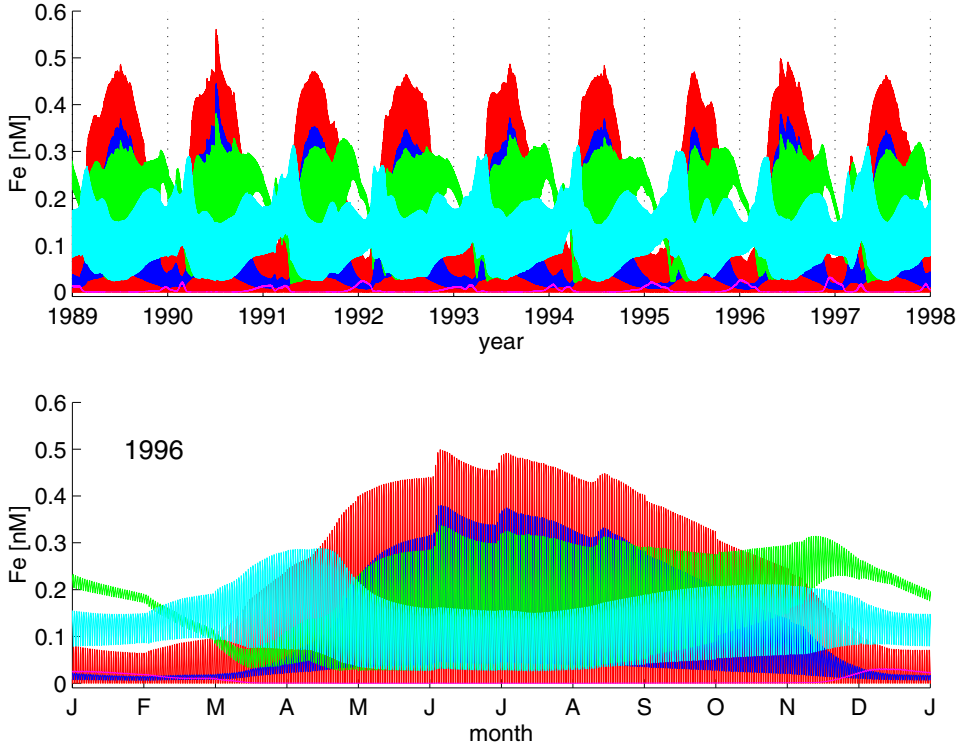

Figure 5. Modeled iron speciation ([Fe(III)′], blue, [Fe(II)′], red; [Fe_{col}], green; [FeL], cyan; [Fe_p], purple). (top) Interannual variability. (bottom) Annual variability (year 1996).

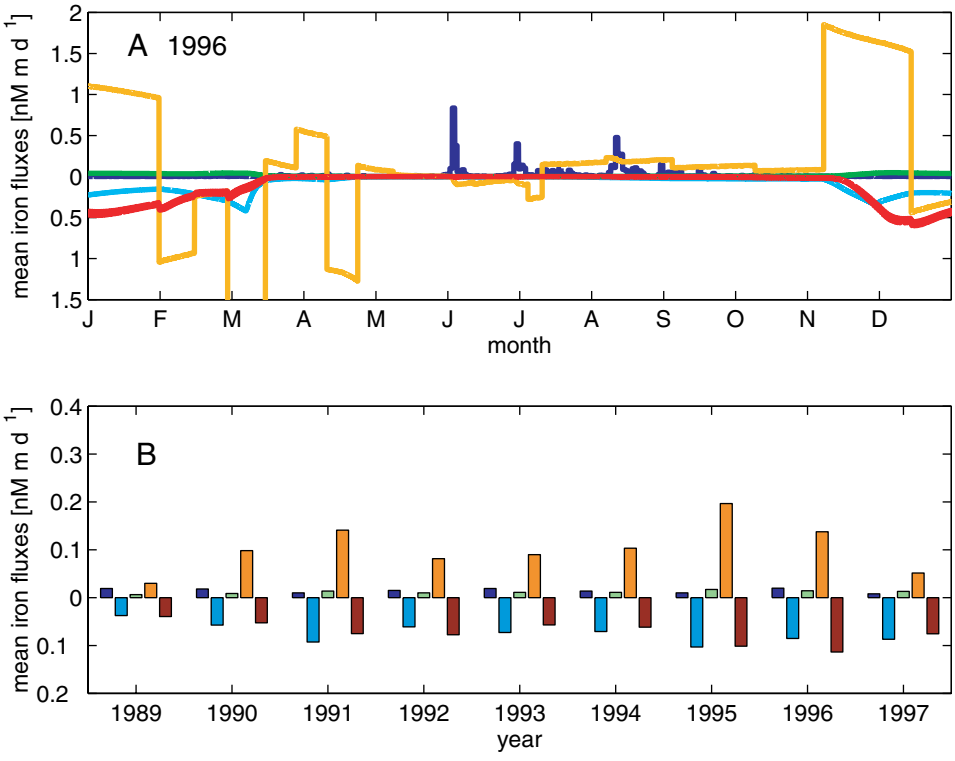

Figure 7. Modeled iron fluxes (dust deposition, blue; biological uptake, light blue; remineralization of biological matter, green; exchange with deeper water, orange; scavenging, brown).

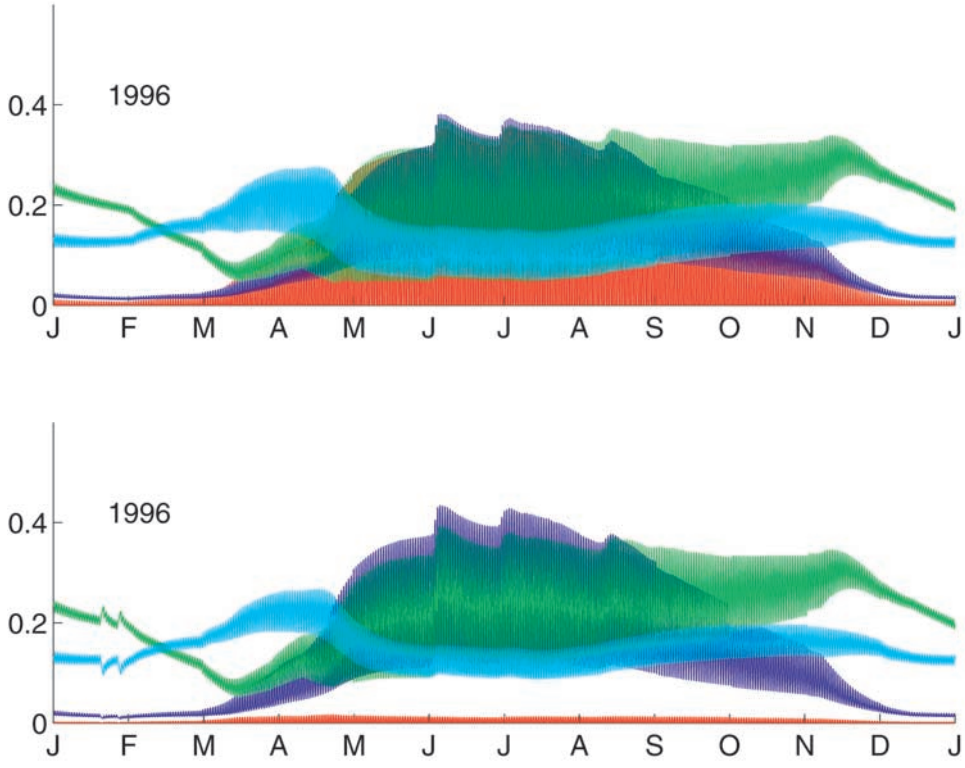

Figure 13. Modeled concentrations of Fe(III)′ (blue), Fe(II)′ (red), Fe_{coll} (green), and FeL (cyan) with catalytic superoxide dismutation by Cu. (top) Experiment Cu1. (bottom) Experiment Cu2.

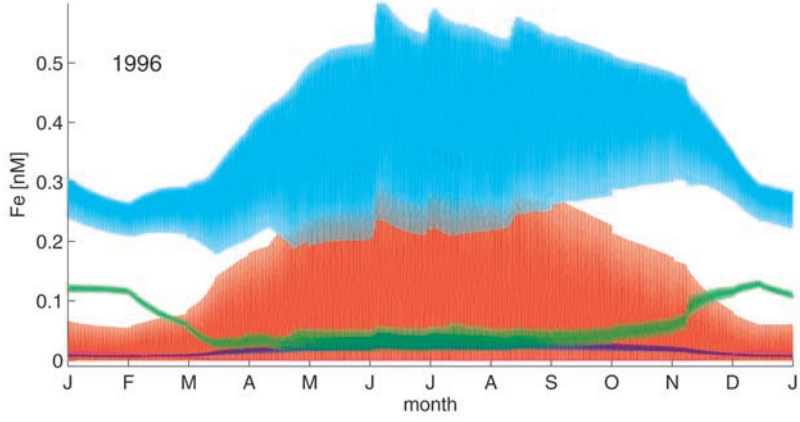

Figure 15. Modeled concentrations of Fe(III)′ (blue), Fe(II)′ (red), Fe_{coll} (green), and FeL (cyan) with permanent excess of organic ligands ($[L_{tot}] \approx 2$ nM) over dissolved iron concentrations.